

Open Source Algorithm for Detecting Sea Ice Surface Features in High Resolution Optical Imagery

Nicholas C. Wright¹, Christopher M. Polashenski^{1,2}

¹Thayer School of Engineering, Dartmouth College, Hanover, NH, USA

²U.S. Army Cold Regions Research and Engineering Laboratories, Hanover, NH, USA

Correspondence to: N. C. Wright (ncwright.th@dartmouth.edu)

Abstract. Snow, ice, and melt ponds cover the surface of the Arctic Ocean in fractions that change throughout the seasons. These surfaces control albedo and exert tremendous influence over the energy balance in the Arctic. Increasingly available m- to dm-scale resolution optical imagery captures the evolution of the ice and ocean surface state visually, but methods for quantifying coverage of key surface types from raw imagery are not yet well established. Here we present an open source system designed to provide a standardized, automated, and reproducible technique for processing optical imagery of sea ice. The method classifies surface coverage into three main categories: Snow and bare ice, melt ponds and submerged ice, and open water. The method is demonstrated on imagery from four sensor platforms and on imagery spanning from spring thaw to fall freeze-up. Tests show the classification accuracy of this method typically exceeds 96%. To facilitate scientific use, we evaluate the minimum observation area required for reporting a representative sample of surface coverage. We provide an open source distribution of this algorithm and associated training data sets and suggest the community consider this a step towards standardizing optical sea ice imagery processing. We hope to encourage future collaborative efforts to improve the code base and to analyze large datasets of optical sea ice imagery.

1 Introduction

The surface of the sea ice-ocean system exhibits many different forms. Snow, ice, ocean, and melt ponds cover the surface in fractions that change throughout the seasons. The relative fractions of these surfaces covering the Arctic ocean are undergoing substantial change due to rapid loss of sea ice (Stroeve et al., 2012), increase in the duration of melt (Markus et al., 2009; Stroeve et al., 2014), decrease in sea ice age (Maslanik et al., 2011), and decrease in sea ice thickness (Kwok and Rothrock, 2009; Laxon et al., 2013) over recent decades. As a whole, the changes are reducing albedo and enhancing the absorption of solar radiation, triggering an ice albedo feedback (Curry et al., 1995; Perovich et al., 2008; Pistone et al., 2014). Large-scale remote sensing has been instrumental in documenting the ongoing change in ice extent (Parkinson and Comiso, 2013), thickness (Kurtz et al., 2013; Kwok and Rothrock, 2009; Laxon et al., 2013), and surface melt state (Markus et al., 2009). An increasing focus on improving prediction of future sea ice and climate states, however, has also created substantial interest in better observing, characterizing, and modeling the *processes* that drive changes in albedo-relevant sea ice surface conditions such as melt pond formation, which occur at smaller length scales. For these, observations that resolve surface conditions explicitly are needed to understand the underlying causes of the seasonal and spatial evolution of albedo in a more sophisticated way.

Explicitly sensing the key aspects of the sea ice surface, including melt pond coverage, degree of deformation, floe size, and lead distributions, requires evaluating the surface at meter to decimeter scale resolution. Variability in the spatial coverage and morphology of these surface characteristics, however, occurs over hundreds of meters to tens of kilometers. Estimates of aggregate scale surface coverage fraction must therefore be made at high resolution over sample domains of many square kilometers. Quantifying the relative abundance of surface types over domains of multi-kilometer scale from manned ground campaigns is both time consuming and impractical. Remote sensing provides a more viable approach for studying these multi-kilometer areas. High resolution optical imagery (e.g. Figure 1) visually captures the surface features of interest, but the methods for analyzing this imagery remain underdeveloped.

The need for remote sensing methods enabling quantification of meter-scale sea ice surface characteristics has been well recognized, and efforts have been made to address it. Recent developments in remote sensing of sea ice surface conditions fall into two categories: (1) methods using low-medium resolution satellite imagery (i.e. having pixel sizes larger than the typical ice surface feature size) with spectral un-mixing type algorithms to derive aggregate measures of sub-pixel phenomena (e.g. for melt ponds Markus et al., 2003; Rösel et al., 2012; Rösel and Kaleschke, 2011; Tschudi et al., 2008) and (2) methods using higher resolution satellite or airborne imagery (i.e. having pixel size smaller than the typical scale of ice surface features) that is capable of explicitly resolving features (e.g. Arntsen et al., 2015; Fetterer and Untersteiner, 1998; Inoue et al., 2008; Kwok, 2014; Lu et al., 2010; Miao et al., 2015; Perovich et al., 2002b; Renner et al., 2014; Webster et al., 2015). The first category, those derived from low-medium resolution imagery, have notable strengths in their frequent sampling and basin-wide coverage. They cannot, however, provide detailed statistics on the morphology of surface features necessary for assessing our process-based understanding and have substantial uncertainty due to ambiguity in spectral signal un-mixing. The second category – observations at high resolutions which explicitly resolve surface properties – can provide these detailed statistics, but were historically limited by a dearth of data acquisitions. Recent increases in imagery availability from formerly classified defense (Kwok, 2014) or commercial satellites (e.g. DigitalGlobe), and increases in manned flights over the Arctic (e.g. IceBridge, SIZRS) have substantially reduced this constraint for optical imagery. Likely increases in collection of imagery from UAV's (DeMott and Hill, 2016) and increases in satellite imaging bandwidth (e.g. DigitalGlobe WorldView 4 launched in 2016) suggest that availability of high resolution imagery will continue to increase.

Processing high resolution sea ice imagery to derive useful metrics quantifying surface state, however, remains a major hurdle. Recent years have seen numerous publications demonstrating the success of various processing techniques for optical imagery of sea ice on limited test cases (e.g. Inoue et al., 2008; Kwok, 2014; Lu et al., 2010; Miao et al., 2015; Perovich et al., 2002b; Renner et al., 2014; Webster et al., 2015). None of these techniques, however, have been adopted as a standard or been used to produce large-scale datasets, and validation has been limited. Furthermore, none have been challenged by imagery collected across the seasonal evolution of the ice or used to process data from multiple sensor platforms. These issues must be addressed to enable in large scale production-type image processing and use of high resolution imagery as a sea ice monitoring tool.

A unique aspect of high resolution sea ice imagery datasets, which differs from most satellite remote sensing, is the quantity of image sources and data owners. Distributed collection and data ownership means centralized processing

of imagery to produce a single product is unlikely. Instead, we believe that distributed processing by dataset owners is more likely and the community therefore has a substantial need for a shared, standard processing protocol. Successful creation of such a processing protocol would increase imagery analysis and result in the production of datasets suitable for ingestion by models to validate surface process parameterizations. In this paper, we assess previous publications detailing image processing methods for remote sensing and present a novel scheme that builds from the strengths and lessons of prior efforts. Our resulting algorithm, the Open Source Sea-ice Processing (OSSP) Algorithm, is presented as a step toward addressing the community need for a standardized methodology, and released in an open source implementation for use and improvement by the community.

We began with three primary design goals that guided our development of the image processing scheme. The method must (1) have a fully automatic workflow and have a low barrier to entry for new users, (2) produce accurate, consistent results in a standardized output format, and (3) be able to produce equivalent geophysical parameters from a range of disparate image acquisition methods. To meet these goals, we have packaged OSSP in a user-friendly format, with clear documentation for start-up. We include a set of default parameters that should meet most user needs, permitting processing of pre-defined image types with minimal set-up. The algorithm parameters are tunable to allow more advanced users to tailor the method to their specific imagery input. We chose an open source format to enhance the ability for the community to explore and improve the code relative to a commercial software. Herein, we discuss how we arrived at the particular technique we use, and why it is superior to some other possible mechanisms. We then demonstrate the ability of this algorithm to analyze imagery of disparate sources by showing results from high resolution DigitalGlobe WorldView satellite imagery in both panchromatic and pansharpened formats, aerial sRGB (standard Red, Green, Blue) imagery, and NASA Operation IceBridge DMS (Digital Mapping System) optical imagery. In this paper, we classify imaged areas into three surface types: Snow and ice, melt ponds and submerged ice, and open water. The algorithm is, however, suitable for classifying any number of categories, should a user be interested in different surface types, and might be adapted for use on imagery of other surface types.

2 Algorithm Design

Two core decisions were faced in the design of this image classification scheme: (1) Whether to analyze the image by individual pixels or to analyze objects constructed of similar, neighboring pixels, and (2) which algorithm to use for the classification of these image units.

Prior work in terrestrial remote sensing applications has shown that object-based classifications are more accurate than single pixel classifications when analyzing high-resolution imagery (Blaschke, 2010; Blaschke et al., 2014; Duro et al., 2012; Yan et al., 2006). In this case, ‘high resolution’ has a specific definition dependent on the relationship between the size of pixels and objects of interest. An image is high resolution when surface features of interest are substantially larger than pixel resolution and therefore are composed of many pixels. In such imagery, objects, or groups of pixels constructed to contain only similar pixels (i.e. a single surface type), can be analyzed as a set. The medium resolution imagery meets this definition for features like melt ponds and ice floes. Object based classification enables an algorithm to extract information about image texture and spatial correlation within the pixel group;

information that is not available in single pixel based classifications and can enhance accuracy of surface type discrimination. Furthermore, object based classifications are much better at preserving the size and shape of surface cover regions. Classification errors of individual pixel schemes tend to produce a ‘speckled’ appearance in the image classification with incorrect pixels scattered across the image. Errors in object based classifications, meanwhile, appear as entire objects that are mislabeled (Duro et al., 2012). Since our intent is to process high-resolution imagery and produce measurements not only of the areal fractions of surface type regions, but also to enable analysis of the size and shape of ice surface type regions (e.g. for floe size or melt pond size determination), the choice of object based classification over pixel based was clear.

A wide range of algorithms were considered for classifying image objects. We first considered the use of supervised versus an unsupervised classification schemes. Unsupervised schemes were rejected as they produce inconsistent, non-intercomparable results. These schemes, such as clustering algorithms, group observations into a predefined number of categories – even if not all feature types of interest are present in an image. For example, an image containing only snow-covered ice will still be categorized into the same number of classes as an image with snow, melt ponds, and open water together – resulting in multiple classes of snow. Since the boundary between classes also changes in each image, standardizing results across imagery with different sources and of scenes with different feature content would be challenging at best.

Supervised classification schemes instead utilize a set of known examples (called training data) to assign a classification to unknown objects based on similarity to user-identified objects. Supervised classification schemes have several advantages. They can produce fixed surface type definitions, allow for more control and fine tuning of the algorithm, improve in skill as more points are added to the training data, and allow users to choose what surface characteristics they wish to classify. While many machine learning techniques have shown high accuracy in remote sensing applications (Duro et al., 2012), we selected a random forest machine learning classifier over other supervised learning algorithms for its ability to handle nonlinear and categorical training inputs (Breiman, 2001; DeFries, 2000; Pal, 2005), resistance to outliers in the training dataset (Breiman, 1996), and relative ease of implementation.

Our scheme, learning from the success of Miao et al. (2015) in classifying aerial imagery, uses an image segmentation algorithm to divide the image into objects which are then classified with random forest machine learning. Our implementation of the segmentation and classification, however, were custom-built using well known image processing tools (Pedregosa et al., 2011; van der Walt et al., 2014) in an open source format. We do not attempt to assert that our method is the optimal method for processing sea ice imagery. Instead, we argue that it is easily usable by the community at large, produces highly accurate and consistent results, and merits consideration as a standardized methodology. In coordination with this publication, we release our code (available at <https://github.com/wrightni/oss> doi:10.5281/zenodo.1133689) with the intention of encouraging movement toward a standardized method. Our hope is to continue development of the algorithm with contributions and suggestions from the sea ice community.

3 Methods

3.1 Image Collection and Preprocessing

The imagery used to test the algorithm was selected from four distinct sources in order to assess the algorithm's ability to deliver consistent and intercomparable measures of geophysical parameters. We chose high resolution satellite imagery from DigitalGlobe's WorldView constellation in panchromatic and 8 band multispectral formats, NASA Operation IceBridge Digital Mapping System optical imagery, and aerial sRGB imagery collected using an aircraft-mounted standard DSLR camera as part of the SIZONet project. We first demonstrate the technique's ability to handle imagery representing all stages of the seasonal evolution of sea ice conditions on a series of 22 panchromatic satellite images collected between March and August of 2014 at a single site in the Beaufort Sea: 72.0° N 128.0° W. We then process 4 multispectral WorldView 2 images of the same site, each collected coincident with a panchromatic image and compare results to assess the benefit of spectral information. Finally, we process a set of 20 sRGB images and 20 IceBridge DMS images containing a variety of sea ice surface types to illustrate the accuracy of the method on aerial image sources. The imagery sources chosen for this analysis were selected to be representative of the variation that exists in optical imagery of sea ice, but there is an abundance of image data that can be processed with this technique.

The satellite images were collected by tasking WorldView 1 and WorldView 2 Digital Globe satellites over fixed locations in the Arctic. Tasking requests were submitted to DigitalGlobe with the support and collaboration of the Polar Geospatial Center. The panchromatic bands of WorldView 1 and 2 both have a spatial resolution of 0.46m at nadir. The WorldView 1 satellite panchromatic band samples the visible spectrum between 400 nm and 900 nm, while the WorldView 2 satellite panchromatic band samples between 450 nm and 850 nm. In addition, WorldView 2 has 8 multispectral bands at 1.84 m nadir resolution, capturing bands within the range of 400nm to 1040nm. Each WorldView image captures an area of ~700-1300 km². Of the 22 useable panchromatic collections at the site, 15 were completely cloud free while 7 of the images were partially cloudy. Images with partial cloud cover were manually masked and cloud covered areas were excluded from analysis. The aerial sRGB imagery was captured along a 100km long transect to the north of Barrow, Alaska with a Nikon D70 DSLR mounted at nadir to a light airplane during June 2009. The IceBridge imagery was collected in July of 2016 near 73° N 171° W with a Canon EOS 5D Mark II digital camera. We utilize the L0 (raw) DMS IceBridge imagery, which has a 10cm spatial resolution when taken from 1500 feet altitude (Dominguez, 2010, updated 2017).

Each satellite image was orthorectified to mean sea level before further processing. Orthorectification corrects for image distortions caused by off-nadir acquisition angles and produces a planimetrically correct image that can be accurately measured for distance and area. Due to the relatively low surface roughness of both multiyear and first year sea ice (Petty et al., 2016), errors induced by ignoring the real topography during orthorectification are small. Multispectral imagery was pansharpened to the resolution of the panchromatic imagery. Pansharpening is a method that creates a high resolution multispectral image by combining intensity values from a higher resolution panchromatic image with color information from a lower resolution multispectral image. The pansharpened imagery used here was created using a 'weighted' Brovey algorithm. This algorithm resamples the multispectral image to the resolution of the panchromatic image, then each pixel's value is multiplied by the ratio of the corresponding panchromatic pixel

value to the sum of all multispectral pixel values. The orthorectification and pansharpening scripts were developed by the Polar Geospatial Center at the University of Minnesota and utilize the GDAL (Geospatial Data Abstraction Library) image processing tools (GDAL, 2016). All imagery used was rescaled to the full 8-bit color space for improved contrast and viewing. No other preprocessing was done to the aerial sRGB imagery or IceBridge DMS imagery.

3.2 Image Segmentation

A flow chart of the image processing steps taken after pre-processing is presented in Fig. 2. The first task in the image processing algorithm is to segment the image into groups of similar pixels, called objects. Accurate segmentation requires finding the boundaries between the natural surface types we wish to differentiate (e.g. the boundary between ice covered and open ocean), delineating their locations, and using these boundaries to produce image objects. Sea ice surface types have large differences in reflectivity and tend to change abruptly, rather than gradually over a large distance. We exploit this characteristic by using an edge detection algorithm to find boundaries between surface types. Figure 3 contains a visual demonstration of this process. First, a Sobel-Feldman operator (van der Walt et al., 2014) is applied to the input image (Fig. 3a). The Sobel-Feldman filter applies a discrete differentiation kernel across the image to find the local gradient of the image intensity. High gradient values correspond to abrupt changes in pixel intensity, which are likely boundaries between surface types. We scale the gradient values by an amplification factor of 2 in order to further highlight edge regions in the image. Following the amplification, we threshold the lowest 10% of the gradient image and set the values to zero. This reduces noise detected by the Sobel-Feldman filter, and eliminates weaker edges. The amplification factor and gradient threshold percentage are both tuning parameters, which can be adjusted to properly segment images based on the input image and the strength of edges sought.

The strongest edges in optical imagery of sea ice are typically the ocean-ice interface, followed by melt pond-ice boundaries, then ice ridges and uneven ice surfaces. In general, the more edges detected, the more segmented the image will become, and the more computational resources required to later classify the increased number of image objects. On the other hand, an under-segmented image may miss the natural boundaries between surfaces. Under segmentation introduces classification error because an object containing two surface types cannot be correctly classified. An optimally segmented image is one which captures all the natural surface boundaries with minimal over-segmentation (i.e. boundaries placed in the middle of features). The appropriate parameters for our imagery were tuned by visual inspection of the segmentation results. In such inspection, desired segmentation lines are manually drawn, and algorithm-determined segmentation lines are overlain and evaluated for completeness.

The result of the edge detection is a gradient map that marks the strength of edges in the image. We use a watershed segmentation technique to build complete objects based on edge locations and intensity (van der Walt et al., 2014). We first calculate all local minimum values in the gradient image, where a marker is then placed to indicate the origin of watershed regions. Each region then begins iteratively expanding in all directions of increasing image gradient until encountering a local maximum in the gradient image or encountering a separately growing region. This continues until every pixel in the image belongs to a unique set. With the proper parameter selection, each object will represent a single surface type. It is often the case that some areas will be over-segmented (i.e. a single surface feature represented

by multiple objects). Over segmentation can either be ignored, or objects can be recombined if they meet similarity criteria in an effort to save computational resources. Here we chose to classify objects without recombination. Figure 3b shows the detected edges overlain on top of the input image.

The watershed segmentation algorithm benefits from the ability to create objects of variable size. Large objects are built in areas of low surface variability while many small objects are created in areas of high variability. This variable object sizing is well suited to sea ice surface classification because the variability of each surface type occurs at different scales. Areas of open water and snow covered first year ice, for example, can often be found in large expanses, while areas that contain melt ponds, ice ridges, or rubble fields frequently cover small areas and are tightly intermingled with other surface types. Variable object sizes give the fine detail needed to capture surfaces of high heterogeneity in their full detail, while limiting over segmentation of uniform areas.

3.3 Segment Classification

3.3.1 Overview

Once the image has been divided into regions of the same surface type, each object must be classified as to which surface type it represents. We classify the objects using a random forest machine learning technique (Breiman, 2001; Pedregosa et al., 2011). The development of a machine learning algorithm requires multiple iterative steps: 1) Select attributes with which to classify each object, 2) create a training dataset, 3) classify unknown image objects based on the training set, and 4) assess performance and refine, starting from step 1. Random forest classifiers excel for their relative ease of use, flexibility in the choice of attributes that define each object, and overall high accuracy even with relatively small training datasets. The random forest classifier is only one of many available machine learning approaches and others may also be suitable.

3.3.2 Surface Type Definitions

Another key challenge to quantitatively monitoring sea ice surface characteristics from high resolution imagery is a lack of standardized surface type definitions. We noted above that high-resolution sea ice imagery comes from many sources; each with different characteristics. As we will see below, each image source will need to have its own training set created by expert human classifiers. The human classifier must train the algorithm according to definitions of each surface type that are broadly agreed upon in the community for the algorithm to be successful in producing intercomparable datasets. While at first the definitions of open water, ice and melt ponds might seem intuitive, many experts in the cryosphere community have differing opinions, especially on transitional states. Deciding where to delineate transitional states is important to standardization. We have established the following definitions for the three surface types we sought to separate, binning transitional states in a manner most consistent with their impact on albedo. Our surface type definitions focus on the behavior of a surface in absorption of shortwave radiation and radiative energy transfer. (1) Open Water (OW): Applied to surface areas that had zero ice cover as well as those covered by an unconsolidated frazil or grease ice. (2) Melt Ponds and Submerged Ice (MPS): Applied to surfaces where a liquid water layer completely submerges the ice. (3) Ice and Snow: Applied to all surfaces covered by snow or bare ice, as well as decaying ice and snow that is saturated, but not submerged. The definition of melt ponds includes the classical

definition of melt ponds where meltwater is trapped in isolated patches atop ice, as well as optically-similar ice submerged near the edge of a floe. While previous work separates these categories (e.g. (Miao et al., 2015) we did not attempt to break these ‘pond’ types because the distinction is unimportant from a shortwave energy balance (albedo) perspective. We further refined the ice and snow category into two sub categories: (3a) Thick Ice and Snow, applied during the freezing season to ice appearing to the expert classifier to be thicker than 50cm or having an optically thick snow cover and to ice during the melt season covered by a drained surface scattering layer (Perovich, 2005) of decaying ice crystals and (3b) Dark and Thin Ice, applied during the freezing season to surfaces of thin ice that are not snow covered including nilas and young ice. This label was also applied during melting conditions to ice covered by saturated slush, but not completely submerged in water. This is ice which in some prior publications (e.g. Polashenski et al., 2012) was labeled as ‘slushy bare ice’. We acknowledge that the boundary between the ice and snow sub-categories is often more a continuum than a defined border but note that distinguishing the two types is useful for algorithm accuracy. Dividing the ice/snow type creates two relatively homogeneous categories rather than a single larger category with large internal differences. A user only interested in the categories of ice, ponds, and open water could simply re-combine them, as we have done for analysis. We created a temporary ‘shadow’ classification category that was used only in panchromatic WorldView images captured prior to melt onset. This category allowed the machine learning algorithm to differentiate dark shadows in spring imagery from melt ponds in summer imagery – surface types that look similar in single-band imagery. This category is used exclusively as a temporary step in processing that allows us to bypass masking shadow regions directly (e.g. (Webster et al., 2015). As this is not designed to be a standalone classification category (as opposed to Miao et al., 2015, 2016), objects classified as a shadow were grouped back with the ice/snow category.

3.3.3 Attribute Selection

Attributes are quantifiable measures of image object properties used by the classifier in discriminating surface types. An enormous array of possible attributes could be calculated for each image object and could be calculated in many ways. Examples of properties that could be quantified as attributes include values of the enclosed pixels, the size and shape of the object, and values of adjacent pixels. The calculation of pixel values aggregated by image objects takes advantage of the additional information held in the pixel group (as compared to individual pixels). We have compiled a list representing a relevant subset of such attributes that can be used to distinguish different surface types in Table 1. We included a selection of attributes similar to those used in previous publications (e.g. Miao et al., 2015), as well as attributes we have developed specifically for our algorithm.

Each image source provides unique information about the surface and it can be expected that a different list of attributes will be optimal for classification of each image type – even though we seek the same geophysical parameters. As high-resolution satellite images can have millions of image objects, calculating the attributes of each object quickly becomes computationally expensive. We have, therefore, determined those that are most valuable for classifying each image type to use in our classification. For example, pansharpened WorldView 2 imagery has 8 spectral bands which can inform the classification, while panchromatic versions of the same image have only a single band. Our goal was to select a combination of attributes that describe the intensity and textural characteristics of the object itself, and of

the area surrounding the object. Table 1 indicates which attributes were selected for use in classifying each image type.

We selected attributes by only including those with a high relative importance. The importance of each attribute is a property of a random forest classifier, and is defined as the number of times a given attribute contributed to the final prediction of an input. After initial tests with large numbers of attributes, we narrowed our selection by using only those attributes that contributed to a classification in greater than 1% of cases. For discussion here, we group the attributes into two broad categories: Those calculated using internal pixels alone (object attributes), and those calculated from external pixel values (neighbor attributes).

3.3.4 Object Attributes

The most important attributes in the classification of an image segment were found to be aggregate measures of pixel intensity within the object. We determine these by analyzing the mean pixel intensity of all bands and the median of the panchromatic band. An important benefit of image segmentation is the ability to calculate estimates of surface texture by looking at the variability within a group of pixels. The texture is often unique in the different surface types we seek to distinguish. Open water is typically uniformly absorptive and has minimal intensity variance. Melt ponds, in contrast, come in many realizations and exhibit a wider range in reflectance, even within individual ponds. To estimate surface texture, we calculate the standard deviation of pixel intensity values and the image entropy within each segment. Image entropy, H , is calculated as

$$H = - \sum p * \log_2 p$$

where p represents the bin counts of a pixel intensity histogram within the segment. We also calculate the size of each segment as the number of pixels it contains. As sea ice surface characteristics evolve appreciably over time, particularly before and after melt onset, we use image acquisition date as an attribute in for classification. While date of melt onset varies, and the reader might argue that a more applicable attribute would be image melt state, melt state, is not an apriori characteristic of the image. It would therefore need to be manually defined, and not meet our demand for a fully automated scheme.

In multispectral imagery, we also calculate the ratios between the mean absorption of each object in certain portions of the spectrum. The important band ratios used for the multispectral WorldView imagery were determined empirically. We tested every possible band combination, and successively removed the ratios that did not contribute to more than 1% of object classifications. In sRGB imagery we use the band ratios shown to be informative in this application by Miao et al. (2015).

In addition to information contained within each object, we utilize information from the surrounding area. To analyze the surrounding region, we determine the dimensions of a minimum bounding box that contains the object, then expand the box by five pixels in each direction. All pixels contained within this box, minus those in the object, are considered to be neighboring pixels. Analogous to the internal attribute calculations, we find the average intensity and standard deviation of these pixels. We also calculate the maximum single intensity within the neighboring region. Searching for attributes outside of the object improves the algorithm's predictive capabilities by providing spatial context. Bright neighboring pixels (as an analog for an illuminated ridge) often provide information to distinguish, for

example, a shadowed ice surface from a melt pond. In panchromatic imagery, melt ponds and shadows appear similar when evaluated solely on internal object attributes. However, a dark region with an immediately adjacent bright region is more likely to be a shadow than a dark region not adjacent to a bright pixel (e.g. a pond). We do note that it is likely that a more complex algorithm, for example identifying those pixels in a radius or distance to the edge of the segment, rather than using a bounding box, would be more reliable. The tradeoff, however, is one of higher computational expense.

3.4 Training Set Creation

Four training datasets were created to analyze the images selected for this paper. One training set was created for each imagery source: Panchromatic satellite imagery, multispectral satellite imagery, aerial sRGB imagery, and IceBridge DMS imagery. Each training set consists of a list of image objects that have been manually classified by a human and a list of attribute values calculated from those objects and their surroundings. The manual classification is carried out by multiple sea ice experts. Experienced observers of sea ice can classify the majority (85%+) of segments in a high resolution optical image with confidence. To address the ambiguity in correct identification of certain segments, however, we used several (4) skilled sea ice observers to repeatedly classify image objects. For the initial creation of our training datasets, two of the users had extensive training in the OSSP algorithm and surface type definitions, while the other two no experience with the algorithm. Users in both categories were briefed on the standard surface type definitions used for this study (section 3.3.2). Figure 4 shows a confusion matrix to compare user classifications. Cells in the diagonal indicate agreement between users, while off-diagonal cells indicate disagreement (Pedregosa et al., 2011). Agreement between the two well-trained users was high (average 94% of segment identifications; Fig. 4a), while the agreement between a well-trained user and a new user was lower (average of 86%; Fig 4b). After an in-person review of the training objects among all four users, the overall agreement rose to 97%. The remaining 3% of objects were cases where the expert users could not agree on a single classification, even after review of the surface type definitions and discussion. These objects were therefore not used in the final training set. Figure 5 shows a series of surface types that span all our classification categories, including those where the classification is clear and those where it is difficult. Difficult segments are over-represented in these images for illustrative purposes, and represent a relatively small fraction of the total surface.

While the skill of the machine learning prediction increases substantially as the size of the training set grows, creating large training sets is time consuming. We found that training datasets of approximately 1000 points yielded accurate and consistent results. We have developed a graphical user interface (GUI) to facilitate the rapid creation of large training sets (see Fig. 6). The GUI presents a user with the original image side by side with an overlay of a single segment on that image. The user assigns a classification to the segment by visual determination.

The training dataset is a critical component of our algorithm because it directly controls the accuracy of the machine learning algorithm – and using a consistent training set is necessary for producing intercomparable results. In coordination with this publication we are releasing our version 1.0 training datasets with the intention that they would represent a first version of *the* standard training set to use with each image type. Though we have found this

training dataset robust through our error analyses below, it is our intention to solicit broader input from the community to refine and expand the training datasets available and release future improved versions.

In addition to cross-validating the creation of a training dataset between users, we assess the quality of our training set through an out-of-bag (OOB) estimate, which is an internal measure of the training set's predictive power. The random forest method creates an ensemble (forest) of classification trees from the input training set. Each classification tree in this forest is built using a random bootstrap sample of the data in the training set. Because training samples are selected at random, each tree is built with an incomplete set of the original data. For every sample in the original training set, there then exists a subset of classifiers that do not contain that sample. The error rate of each classifier when used to predict the samples that were left out is called the OOB estimate (Breiman, 2001). The OOB estimate has been shown to be equivalent to predicting a separate set of features and comparing the output to a known classification (Breiman, 1996).

3.5 Assigning Classifications

Once the training dataset is complete, the algorithm is prepared to predict the classification of unknown objects in the images. The random forest classifier is run and a classified image is created by replacing the values within each segment by the classification label predicted. Figure 3c shows the result of labeling image objects with their predicted classification. From the classified image, it is possible to produce a number of useful statistics. The most basic measurement is the total pixel counts for each of the three surface categories. This provides both the total area, in square kilometers, that each surface covers, and the fraction of each image that is covered by each surface type. It would also be possible to calculate measurements such as the average segment size for each surface, melt pond size and connectivity, or floe size distributions. Each of these, however, has its own standardization problems significant enough to merit their own paper.

For demonstration, we have used the output from our image classification to calculate the fractional melt pond coverage for each date. The melt pond fraction was defined as the area of melt ponds and submerged ice divided by the total area covered by ice floes, i.e.:

$$\text{Melt Pond Coverage} = \frac{\text{Area}_{MPS}}{\text{Area}_{MPS} + \text{Area}_{I+S}}$$

where the subscript MPS indicates predicted melt ponds and submerged ice and I+S indicates predicted ice and snow.

3.6 Determining Classification Accuracy

The primary measure of classification accuracy was to test the processed imagery on a per pixel basis against human classification. For every processed image, we selected a simple random sample of 100 pixels chosen from the whole image and asked four sea ice experts to assign a classification to those pixels. For a single image from each image source we also asked the sea ice experts to classify and additional 900 pixels. This larger sample was created to demonstrate a tighter confidence interval, while the smaller samples were chosen to demonstrate consistency across images. We used the same GUI developed to create training datasets to assess pixel accuracy. Pixels were presented at random to the user by showing the original image with the given pixel highlighted. The user then identified which

of the surface type categories best described that pixel. This assignment is then compared to the algorithm's prediction behind the scenes. The accuracy, as determined by each of the four experts, was averaged to create a composite accuracy for each image.

4 Results

4.1 Classification of Four Imagery Sources

The OSSP image processing method proved highly suitable for the task of classifying sea ice imagery. A visual comparison between the raw and processed imagery, shown in Fig. 7 can quickly demonstrate this in a qualitative sense. Figure 7 contains a comparison between the original and classified imagery for each source, selected to show the performance of the algorithm on images that contain a variety of surface types. The colors shown correspond to the classification category; regions colored black are open water, blue regions are melt ponds and submerged ice, gray regions are wet and thin ice, and white regions are snow and ice. The quantitative processing results, including surface distributions and classification accuracy are shown in Table 2. The overall classification accuracy was $96 \pm 3\%$ across 20 IceBridge DMS images; $95 \pm 3\%$ across 20 aerial sRGB images; $97 \pm 2\%$ across 22 panchromatic WorldView 1 and 2 images; and $98 \pm 2\%$ across 4 multispectral WorldView 2 images.

The nature of the classification error is presented using a confusion matrix that compares the algorithm classification with a manual classification for 1000 randomly selected pixels. Four confusion matrices, one for a single image from each of the four image sources is shown in Fig. 8. Values along the diagonal of the square are the classifications where the algorithm and the human observer agreed, while values in off-diagonal areas indicate disagreement. Concentration of error into a particular off-diagonal cell helps illustrate the types of confusion the algorithm experiences. The number of pixels that fall into off-diagonal cells is low across all imagery types. In the IceBridge imagery, there is a slight tendency for the algorithm to classify surfaces as open water where a human would choose melt pond. This is caused by exceptionally dark melt ponds on the edge of melting through (Fig. 5, panels F and I). Classification of multispectral WorldView imagery has a small bias towards classifying melt ponds over dark or thin ice (Fig. 5, panel D). Aerial sRGB and Panchromatic WorldView images do not have a distinct pattern to their classification errors.

The internal metric of classification training dataset strength, the Out of Bag Error (OOB) estimates, on a 0.0 to 1.0 scale, are shown in Table 3 for the trees built from our three training sets. The OOB estimate represents the mean prediction error of the random forest classifier, i.e. an OOB score of 0.92 estimates that the decision tree would predict 92% of segments that are contained in the training dataset correctly. The discrepancy between OOB error and the overall classification accuracy is a result of more frequent misclassification of smaller objects; overall accuracy is area weighted, while the OOB score is not.

4.2 WorldView: Analyzing A Full Seasonal Progression

We analyzed 22 images at a single site in the Beaufort Sea collected between March and August of 2014 to challenge the method with images that span the seasonal evolution of ice surface conditions. The site is Eulerian; it observes a

single location in space rather than following a single ice floe through its lifecycle as it drifts. Still, the results of these image classifications (shown in Fig. 9) illustrate the progression of the ice surface conditions in terms of our four categories over the course of a single melt season. While cloud cover impacted the temporal continuity of satellite images collected at this site, we are still able to follow the seasonal evolution of surface features. A time series of fractional melt pond coverage calculated from the satellite image site is plotted in Fig. 10. The melt pond coverage jumps to 22% in the earliest June image, as initial ponding begins and floods the surface of the level first year ice. This is followed by a further increase to 45% coverage in the next few days. The melt pond coverage then drops back down to 30% as melt water drains from the surface and forms well defined ponds. The evolution of melt pond coverage over our satellite observation period is consistent with prior field observations (Eicken, 2002; Landy et al., 2014; Polashenski et al., 2012) and matches the four stages of ice melt first described by Eicken (2002). The ice at this observation site fully transitions to open water by mid-July, though it appears that the ice is advected out of the region in the late stages of melt rather than completing melt at this location.

5 Discussion

5.1 Error

There are four primary sources of error in the OSSP method as presented, two internal to the method and two external. Internal error is caused by segment misclassification and by incomplete segmentation (i.e. leaving pixels representing two surface types within one segment). The net internal error was quantified in section 3.6 and 4. External error is introduced by pixilation – or blurring of real surface boundaries due to insufficient image resolution – and human error in assigning a ‘ground truth’ value to an aerial or satellite observation during training.

5.1.1 Internal Error

Through assessing the accuracy of each classified image on a pixel-by-pixel basis (section 3.6), we collect all internal sources of error into one measurement: The algorithm either assigned the same classification as a human would have, or it did not. Total internal accuracy calculated for the method, relative to human classifiers, is quite good, at 90-99% across all image types. Our experience is that this level of accuracy approaches the accuracy with which fractional surface coverage can practically be determined from labor intensive ground campaign techniques such as lidar and measured linear transects (e.g. Polashenski et al., 2012)

The first type of internal error is misclassification error, where the image classification algorithm fails to assign the same classification that a human expert would choose. This type of error is best quantified by analyzing the training datasets. The OOB score for each forest of decision trees (Table 3) provides an estimate of each forest’s ability to correctly predict objects similar to those used to create the forest (section 3.4). The OOB score is not influenced by segmentation error, because the objects selected for training dataset use were filtered to remove any objects that contained more than one surface type. The most commonly misapplied category was the Dark and Thin Ice subcategory of Ice and Snow. This category often represents surface types that are in a transitional state, and is often difficult to classify even for a human observer.

The second type of internal error is segmentation error, where an object is created that contains more than one of the surface types we are trying to distinguish. This occurs when boundaries between objects are not placed where boundaries between surfaces exist; an issue most common where one surface type gradually transitions to another. When this occurs, some portion of that object will necessarily be misclassified. We have compensated for areas that lack sharp boundaries by biasing the image segmentation towards over-segmentation, but a small number of objects still contain more than one surface type. During training set creation, we asked the human experts to identify objects containing more than one surface type. 3.5% of objects were identified as insufficiently segmented in aerial imagery, and 2% of objects in satellite imagery. This represents the upper limit for the total percentage of insufficiently segmented objects for several reasons. First, segmentation error was most prevalent in transitional surface types (i.e. Dark and Thin Ice), which represents a small portion of the overall image and is composed of relatively small objects. This category is overrepresented in the training objects because objects were chosen to sample each surface type and not weighted by area. In addition, insufficiently segmented objects are generally composed of only two surface types, and end up identified as the surface which represents more of the object's area. Hence the total internal error introduced by segmentation error is appreciably smaller than misclassification error, likely well under 1%.

5.1.2 External Error

The first form of external error is introduced by image resolution. At lower image resolutions, more pixels of the image span edges, and smaller features are more likely to go undetected. Pixels on the edge of surface types necessarily represent more than one surface type, but can be classified as only one. Misclassification of these has the potential to become a systemic error if edge pixels were preferentially placed in a particular category. We assessed this error's impact by taking high resolution IceBridge imagery (0.1m), downsampling to progressively lower resolution, and reprocessing. Figure 11 shows the surface type percentages for three IceBridge images at decreasing resolution. Figure 12 shows a series of downsampled images and their classified counterparts. Surprisingly, despite clear pixilation and aliasing in the imagery, little change in aggregate classification statistics occurred as resolution was lowered from 0.1 to 2m. This suggests that at resolutions used for this paper, edge pixels do not significantly impact the classification results. It may also be possible to forego the pansharpening process discussed in section 3.1, and use 2m multispectral WorldView imagery directly.

The second type of external error occurs when the human expert fails to correctly label a segment. Even skilled human observers cannot classify every pixel in the imagery definitively, and indeed the division between the surface types can sometimes be indistinct even to an observer on the ground. We addressed this concern by employing observers extensively trained in the sea ice field, both in remote sensing and in-situ observations, comparing multiple human classifications of the same segments. After discussion, the portion of image objects subject to human observer disagreement or uncertainty is small. Human observers disagreed on 3% of objects creating our training sets. The possibility of systemic bias among the expert observer classifications cannot be excluded because real ground truth, in the form of geo-referenced ground observations from knowledgeable observers was, unfortunately, not available for any of the imagery. Conducting this type of validation would be helpful, but given high confidence human expert classifiers expressed in their classifications and low disagreement between them, may not be essential.

5.1.3 Overall Error

The fact that misclassification dominates the internal error metric suggests that error could be reduced if additional object attributes used by human experts to differentiate surface types could be identified. The agreement between the OSSP method and a human (96% \pm 3%) is similar to the agreement between different human observers (97%), meaning that the algorithm is nearly as accurate as a human manually classifying an entire image. If we exclude the possibility for systemic error in human classification, and assume other errors are unrelated to one another, we can calculate a total absolute accuracy in surface type determination as approximately 96%.

5.2 Producing Derived Metrics of Surface Coverage

The classified imagery, presented as a raster, (e.g. Fig. 7) is not likely to be the end product used in many analyses. Metrics of the sea ice state in simpler form will be calculated. We already introduced the most basic summary metrics in section 4, where we presented fractional surface coverage calculated from the total pixel counts for each of the four surface categories in each image. We also presented the calculation of melt pond coverage as a fraction of the ice-covered portion of the image, rather than total image area. The calculation of these is straightforward. Other metrics commonly discussed in the literature that could be produced with minimal additional processing include those capturing melt pond size, connectivity, or fractal dimension, as well as floe size distribution or perimeter to area ratio. As with definitions of surface type, standardizing metrics will be necessary to produce intercomparable results. We discussed the more complex metrics which could be derived from this imagery with several other groups. We determined that standardizing these and other more advanced metrics will require more input and consensus building before a community standard can be suggested. We leave determining standard methods for calculating these more complex metrics to a future work.

Equipped with the images processed by OSSP, we consider what size area must be imaged, classified, and summarized to constitute ‘one observation’ and how regionally representative such an observation is. Even with the increasing availability of high resolution imagery, it is unlikely that high resolution imaging will regularly cover more than a small portion of the Arctic in the near future. As a result, high resolution image analysis will likely remain a ‘sampling’ technique. Since the scale of sea ice heterogeneity varies for each property type, a minimum area unique to that property must be analyzed to qualify as a representative sample of the surface conditions. Finding that minimum area involves addressing the ‘aggregate scale’ – the area over which a measured surface characteristic becomes uniform and captures a representative average of the property in the area (Perovich, 2005). It may also be possible to determine an aggregate scale statistic within well constrained bounds by random sub-sampling of the region, and therefore reduce processing time. Here we conduct analysis of these sampling concepts and suggest this analysis of the aggregate scale be conducted for any metric.

First, we sought to determine the aggregate scale for the simple fractional coverage metrics of ice as a fraction of total area and melt pond as a fraction of ice area. This would inform us, for example, as to whether processing the entire area of a WorldView image (up to 1000km²) was necessary, or alternatively if a full WorldView image was sufficient to constitute a sample. First, we evaluated the convergence of fractional coverage within areas of increasing size towards the image mean. For a WorldView image depicting primarily first year ice in various stages of melt, we

created non-overlapping gridded subsections and determined the fractional coverage within each grid cell. The size of grid cells was varied logarithmically from 100×100 pixels (10^2) to 31622×31622 pixels ($10^{4.5}$) or from 0.0025 km^2 to 250 km^2 . For each sample size, we gridded the image and evaluated every subsection within the entire image. Figure 13a shows a scatterplot of the fractional melt pond coverage in each image grid plotted against the log of total area of that grid cell. As the area sampled increases, the melt pond fraction shows lower deviation from the mean, as expected. To assist in evaluating the convergence towards the mean, we plot the 95% prediction interval for each image subset size in Fig. 13a (large red dots). The range of pond fraction values between these two points represents the interval within which 95% of samples of this size would fall. The width of the 95% prediction interval declines linearly with respect to sample area in log space, shrinking by 0.3 for each order of magnitude that sample area increases. Visually, it appears that maximum convergence may have been reached at a sample area of $\sim 30 \text{ km}^2$ ($\sim 10^{1.5} \text{ km}^2$), though there are an insufficient number of samples at this large area within a single image to be certain. Regardless of whether convergence is complete, the prediction interval tells us that at 30 km^2 , 95% of areas sampled could be expected to have pond coverage within 5% of the mean of a full image ($\sim 1000 \text{ km}^2$). This is consistent with prior work that indicated the aggregate scale for melt pond fraction determination is on the order of several tens of square kilometers (Perovich, 2005; Perovich et al., 2002a). In Fig. 13b we conduct the same analysis for the total ice-covered fraction (ponded + unponded ice) of the image. We see the range of the prediction interval generally drops as larger samples are taken, but does not converge as cleanly or quickly as the pond coverage prediction interval does - a finding that is unsurprising as ice fraction is composed of discrete floes with sizes much larger than melt ponds. The limited convergence indicates that the aggregate scale for determination of ice covered fraction is at least on the order of the scale of a WorldView image, and likely larger. Aggregate scale ice concentration, unlike melt pond fraction, is a statistic better observed with medium resolution remote sensing platforms such as MODIS or Landsat due to the need for a larger satellite footprint. WorldView imagery may be particularly useful for determining smaller scale parts of floe size distributions or for validating larger scale remote sensing of ice fraction, if the larger scale pixels can be completely contained within the worldview image. Floe size distribution will likely require nesting of scales in order to fully access both large and small-scale parts of the floe size distribution.

We next investigated whether it is possible to reduce the processing load required to determine the melt pond or ice fraction of an image within certain error bounds by processing collections of random image subsets. To do this, it is useful to first establish two definitions: (1) one random sample of size N represents N randomly selected 100×100 pixel boxes, and (2) one adjacent sample of size N is a single area with size $100\sqrt{N} \times 100\sqrt{N}$. In other words, a random sample and an adjacent sample both represent an image area of $10,000 \times N$ pixels, but consist of independent and correlated pixels, respectively. We expect random samples to better represent the total image mean melt pond fraction because ice conditions are spatially correlated and a single large area is not composed of independent samples. We evaluated this hypothesis by collecting 1000 random and adjacent samples of size $N=100$, with replacement. Results are shown in Fig. 14. In Figure 14a, we plot a histogram of the mean melt pond fraction determined from these 1000 samples. The means determined from sets that contained randomly distributed image areas, are in red. The means determined from sets of adjacent image areas are in blue. Although both sets represent samples of the same total image

area, the one composed of independent subsets randomly selected from across the image does a much better job of representing the mean value, with a smaller standard deviation.

Estimating the mean of a complete image by sampling randomly selected areas of the image becomes a simple statistics problem. The sample size needed to estimate a population mean to within a certain confidence interval and margin of error can be determined with the formula:

$$n = \left(\frac{Z\sigma}{ME} \right)^2$$

where n is the sample size, Z is the z-score for the confidence interval required, σ is the population standard deviation, and ME is the margin of error. The standard deviation of random samples with size 100 is ~ 0.2 (Fig 14b). Assuming a 95% confidence interval ($Z=1.96$), and a margin of error of 5%, a sample size of 64 is required. In other words, with 64 random samples of size 100 we can predict the mean melt pond fraction of the total image with 95% confidence to within 5%. 64 samples of size 100 corresponds to an image area of $\sim 16\text{km}^2$, significantly smaller than the total image size.

In order to show these results visually, we return to Fig. 13 and place another set of 95% prediction interval bounds (purple dots). These bounds represent the prediction interval for a random sample of size necessary for the total area to equal the area on the x axis. The result is quite powerful. By processing as little as 16km^2 of the image, collected from samples randomly distributed across the area, we can determine aggregate melt pond fraction to within 5% of the true value with a confidence of 95%. We estimate that this 5% margin of error is comparable to the sum of internal (2-4%) and external errors in our processing algorithm (section 5.1). For large scale processing we suggest that when the sample confidence interval is below the image processing technique accuracy, sampling of larger areas is no longer necessary.

A similar analysis is presented in Fig. 14c and 14d for ice fraction. While the WorldView image is likely not large enough to represent the aggregate scale for ice fraction, randomly sampling the image still provides an expedient way to determine the mean ice fraction of the image within certain bounds, while processing only a small fraction of the image. Calculating the 95% prediction interval of random samples representing the total image area shown on the x axis (purple dots) again shows that the total image mean can be estimated by calculating only a small portion of the total image.

These explorations of image sampling permit us to recommend that users can estimate the total image pond fraction by selecting N sets of 100 randomly selected $50\text{x}50\text{m}$ regions (where N is selected to provide the desired confidence interval and margin of error). We suggest a standard, which incorporates some ‘safety factor’, for processing imagery to produce estimates of melt pond fraction should be to process 25km^2 of area contained in at least 100 randomly located image subsets from domains of at least 100km^2 . We note that flying a UAV over a domain and collecting imagery along flight tracks will not count as fully ‘random’ in this context, since the images along-track are spatially correlated. Since an image does not represent the aggregate scale for ice fraction, we cannot recommend a specific sampling strategy for the aggregate scale, but note that processing of 25km^2 of imagery from randomly distributed subsets produces a prediction interval around the mean of approximately the same size as the upper limit of uncertainty for our image processing technique. The statistical approach for determining aggregate statistics should not depend

on the seasonality of the image nor the type of image used so long as the total area observed is sufficiently greater than the variability in the surface feature being investigated. However, these recommendations should be considered provisional, because they are subject to impacts from differences in ice property correlation scales, and should be further evaluated for accuracy as larger processed datasets are available.

5.3 Community Adoption

We have provided a free distribution of the OSSP algorithm and the training sets discussed in section 3.4 and 4 as a companion to this publication, complete with detailed startup guides and documentation. This OSSP algorithm has been implemented entirely in Python using open source resources with release to additional users in mind. The code, along with documentation, instructional guidelines, and premade training sets (those used for the analyses herein) is available at <https://github.com/wrightni/ossdp> (doi:10.5281/zenodo.1133689). The software is packaged with default parameters and version controlled training sets for 4 different imagery sources. The package includes a graphical user interface to allow users to build custom training datasets that suit their individual needs. The algorithm was constructed with the flexibility to allow for the classification of any number of features given an appropriate training dataset.

Our intention is that by providing easy access to the code in an open source format, we will enable both specific inquiries and larger scale image processing that supports community efforts at general sea ice monitoring. We plan to continue improving and updating the code as it gains users and we receive community feedback. We hope to encourage others to design their own features and add-ons. Since the predictive ability of the machine learning algorithm improves as more training data is added, we wish to strongly encourage the use of the GUI to produce additional training sets and we plan to collate other users training sets into improved training versions. See documentation of the training set creation GUI for more information on how to share a training set.

The OSSP algorithm helps to bring the goal of having a standardized method for deriving geophysical parameters from high resolution optical sea ice imagery closer to reality. In the larger picture, developing such a tool is only the first step. We recall that the motivation behind this development was the need to quantify sea ice surface conditions in a way that could enable better understanding of the processes driving changes in sea ice cover. The value of the toolkit will only be realized if it is used for these scientific inquiries. We look forward to working with imagery owners to facilitate processing of additional datasets.

6. Conclusions

We have implemented a method for classifying the sea ice surface conditions from high resolution optical imagery of sea ice. We designed the system to have a low barrier to entry, by coding it in an open source format, providing detailed documentation, and releasing it publicly for community use. The code identifies the dominant surface types found in sea ice imagery; open water, melt ponds and submerged ice, and snow and ice, with accuracy that averages 96 percent – comparable to the consistency between manual expert human classifications of the imagery. The algorithm is shown to be capable of classifying imagery from a range of image sensing platforms including panchromatic and pansharpened WorldView satellite imagery, aerial sRGB imagery, and optical DMS imagery from

NASA IceBridge missions. Furthermore, the software can process imagery collected across the seasonal evolution of the sea ice from early spring through complete ice melt, demonstrating it is robust even as the characteristics of the ice features seasonally evolve. We conclude, based on our error analysis, that this automatic image processing method can be used with confidence in analyzing the melt pond evolution at remote sites.

With appropriate processing, high resolution imagery collections should be a powerful tool for standardized and routine observation of sea ice surface characteristics. We hope that providing easy access to the methods and algorithm developed herein, we will facilitate the sea ice community convergence on a standardized method for processing high resolution optical imagery either by adoption of this method, or by suggestion of an alternate method complete with code release and error analysis.

The authors declare that they have no conflict of interest.

Data Availability. The OSSP algorithm code is available from <https://github.com/wrightni/oss> (doi:10.5281/zenodo.1133689). Image data and processing results are available at the NSF Arctic Data Center (ADC). Raw and preprocessed image data from DigitalGlobe WorldView images are not available due to copyright, but can be acquired from DigitalGlobe or the Polar Geospatial Center at the University of Minnesota.

Acknowledgements. This work was supported by the Office of Naval Research Award N0001413MP20144 and the National Science Foundation Award PLR-1417436. We would like to thank Donald Perovich and Alexandra Arntsen for their assistance in creating machine learning training datasets. We would also like to thank Arnold Song, Justin Chen, and Elias Deeb for their assistance and guidance with the development of the OSSP code. WorldView satellite imagery was provided with the DigitalGlobe NextView License through the University of Minnesota Polar Geospatial Center. A collection of the aerial imagery was collected by the SIZONet project. Some data used in this paper were acquired by the NASA Operation IceBridge Project.

References

- Arntsen, A. E., Song, A. J., Perovich, D. K. and Richter-Menge, J. A.: Observations of the summer breakup of an Arctic sea ice cover, *Geophys. Res. Lett.*, 42(19), 8057–8063, doi:10.1002/2015GL065224, 2015.
- Blaschke, T.: Object based image analysis for remote sensing, *ISPRS J. Photogramm. Remote Sens.*, 65(1), 2–16, doi:10.1016/j.isprsjprs.2009.06.004, 2010.
- Blaschke, T., Hay, G. J., Kelly, M., Lang, S., Hofmann, P., Addink, E., Queiroz Feitosa, R., van der Meer, F., van der Werff, H., van Coillie, F. and Tiede, D.: Geographic Object-Based Image Analysis – Towards a new paradigm, *ISPRS J. Photogramm. Remote Sens.*, 87, 180–191, doi:10.1016/j.isprsjprs.2013.09.014, 2014.
- Breiman, L.: Bagging Predictors, *Mach. Learn.*, 24(2), 123–140, doi:10.1023/A:1018054314350, 1996.
- Breiman, L.: Random Forests, *Mach. Learn.*, 45(1), 5–32, doi:10.1023/A:1010933404324, 2001.

- Curry, J. A., Schramm, J. L. and Ebert, E. E.: Sea ice-albedo climate feedback mechanism, *J. Clim.*, 8(2), 240–247, doi:10.1175/1520-0442(1995)008<0240:SIACFM>2.0.CO;2, 1995.
- DeFries, R. .: Multiple Criteria for Evaluating Machine Learning Algorithms for Land Cover Classification from Satellite Data, *Remote Sens. Environ.*, 74(3), 503–515, doi:10.1016/S0034-4257(00)00142-5, 2000.
- DeMott, P. J. and Hill, T. C. J.: Investigations of Spatial and Temporal Variability of Ocean and Ice Conditions in and Near the Marginal Ice Zone. The “Marginal Ice Zone Observations and Processes Experiment” (MIZOPEX) Final Campaign Summary, DOE ARM Climate Research Facility, Pacific Northwest National Laboratory; Richland, Washington., 2016.
- Dominguez, R.: IceBridge DMS L0 Raw Imagery, Version 1, , doi:10.5067/UMFN22VHGGMH, 2010.
- Duro, D. C., Franklin, S. E. and Dubé, M. G.: A comparison of pixel-based and object-based image analysis with selected machine learning algorithms for the classification of agricultural landscapes using SPOT-5 HRG imagery, *Remote Sens. Environ.*, 118, 259–272, doi:10.1016/j.rse.2011.11.020, 2012.
- Eicken, H.: Tracer studies of pathways and rates of meltwater transport through Arctic summer sea ice, *J. Geophys. Res.*, 107(C10), 8046, doi:10.1029/2000JC000583, 2002.
- Fetterer, F. and Untersteiner, N.: Observations of melt ponds on Arctic sea ice, *J. Geophys. Res. Ocean.*, 103(C11), 24821–24835, doi:10.1029/98JC02034, 1998.
- GDAL: GDAL - Geospatial Data Abstraction Library, Version 2.1.0, Open Source Geospatial Found. [online] Available from: <http://gdal.org>, 2016.
- Inoue, J., Curry, J. A. and Maslanik, J. A.: Application of Aerosondes to Melt-Pond Observations over Arctic Sea Ice, *J. Atmos. Ocean. Technol.*, 25(2), 327–334, doi:10.1175/2007JTECHA955.1, 2008.
- Kurtz, N. T., Farrell, S. L., Studinger, M., Galin, N., Harbeck, J. P., Lindsay, R., Onana, V. D., Panzer, B. and Sonntag, J. G.: Sea ice thickness, freeboard, and snow depth products from Operation IceBridge airborne data, *Cryosph.*, 7(4), 1035–1056, doi:10.5194/tc-7-1035-2013, 2013.
- Kwok, R.: Declassified high-resolution visible imagery for Arctic sea ice investigations: An overview, *Remote Sens. Environ.*, 142, 44–56, doi:10.1016/j.rse.2013.11.015, 2014.
- Kwok, R. and Rothrock, D. A.: Decline in Arctic sea ice thickness from submarine and ICESat records: 1958–2008, *Geophys. Res. Lett.*, 36(15), n/a-n/a, doi:10.1029/2009GL039035, 2009.
- Landy, J., Ehn, J., Shields, M. and Barber, D.: Surface and melt pond evolution on landfast first-year sea ice in the Canadian Arctic Archipelago, *J. Geophys. Res. Ocean.*, 119(5), 3054–3075, doi:10.1002/2013JC009617, 2014.
- Laxon, S. W., Giles, K. A., Ridout, A. L., Wingham, D. J., Willatt, R., Cullen, R., Kwok, R., Schweiger, A., Zhang, J., Haas, C., Hendricks, S., Krishfield, R., Kurtz, N., Farrell, S. and Davidson, M.: CryoSat-2 estimates of Arctic sea ice thickness and volume, *Geophys. Res. Lett.*, 40(4), 732–737, doi:10.1002/grl.50193, 2013.
- Lu, P., Li, Z., Cheng, B., Lei, R. and Zhang, R.: Sea ice surface features in Arctic summer 2008: Aerial observations, *Remote Sens. Environ.*, 114(4), 693–699, doi:10.1016/j.rse.2009.11.009, 2010.
- Markus, T., Cavalieri, D. J., Tschudi, M. A. and Ivanoff, A.: Comparison of aerial video and Landsat 7 data over ponded sea ice, *Remote Sens. Environ.*, 86(4), 458–469, doi:10.1016/S0034-4257(03)00124-X, 2003.

Markus, T., Stroeve, J. C. and Miller, J.: Recent changes in Arctic sea ice melt onset, freezeup, and melt season length, *J. Geophys. Res.*, 114(C12), C12024, doi:10.1029/2009JC005436, 2009.

Maslanik, J., Stroeve, J., Fowler, C. and Emery, W.: Distribution and trends in Arctic sea ice age through spring 2011, *Geophys. Res. Lett.*, 38(13), doi:10.1029/2011GL047735, 2011.

Miao, X., Xie, H., Ackley, S. F., Perovich, D. K. and Ke, C.: Object-based detection of Arctic sea ice and melt ponds using high spatial resolution aerial photographs, *Cold Reg. Sci. Technol.*, 119, 211–222, doi:10.1016/j.coldregions.2015.06.014, 2015.

Miao, X., Xie, H., Ackley, S. F. and Zheng, S.: Object-Based Arctic Sea Ice Ridge Detection From High-Spatial-Resolution Imagery, *IEEE Geosci. Remote Sens. Lett.*, 13(6), 787–791, doi:10.1109/LGRS.2016.2544861, 2016.

Pal, M.: Random forest classifier for remote sensing classification, *Int. J. Remote Sens.*, 26(1), 217–222, doi:10.1080/01431160412331269698, 2005.

Parkinson, C. L. and Comiso, J. C.: On the 2012 record low Arctic sea ice cover: Combined impact of preconditioning and an August storm, *Geophys. Res. Lett.*, 40(7), 1356–1361, doi:10.1002/grl.50349, 2013.

Pedregosa, F., Varoquaux, G., Gramfort, A., Michel, V., Thirion, B., Grisel, O., Blondel, M., Prettenhofer, P., Weiss, R., Dubourg, V., Vanderplas, J., Passos, A., Cournapeau, D., Brucher, M., Perrot, M. and Duchesnay, É.: Scikit-learn: Machine Learning in Python, *J. Mach. Learn. Res.*, 12(Oct), 2825–2830 [online] Available from: <http://jmlr.csail.mit.edu/papers/v12/pedregosa11a.html> (Accessed 24 July 2017), 2011.

Perovich, D. K.: On the aggregate-scale partitioning of solar radiation in Arctic sea ice during the Surface Heat Budget of the Arctic Ocean (SHEBA) field experiment, *J. Geophys. Res.*, 110(C3), C03002, doi:10.1029/2004JC002512, 2005.

Perovich, D. K., Tucker, W. B. and Ligett, K. A.: Aerial observations of the evolution of ice surface conditions during summer, *J. Geophys. Res.*, 107(C10), 8048, doi:10.1029/2000JC000449, 2002a.

Perovich, D. K., Grenfell, T. C., Light, B. and Hobbs, P. V.: Seasonal evolution of the albedo of multiyear Arctic sea ice, *J. Geophys. Res.*, 107(C10), 8044, doi:10.1029/2000JC000438, 2002b.

Perovich, D. K., Richter-Menge, J. A., Jones, K. F. and Light, B.: Sunlight, water, and ice: Extreme Arctic sea ice melt during the summer of 2007, *Geophys. Res. Lett.*, 35(11), L11501, doi:10.1029/2008GL034007, 2008.

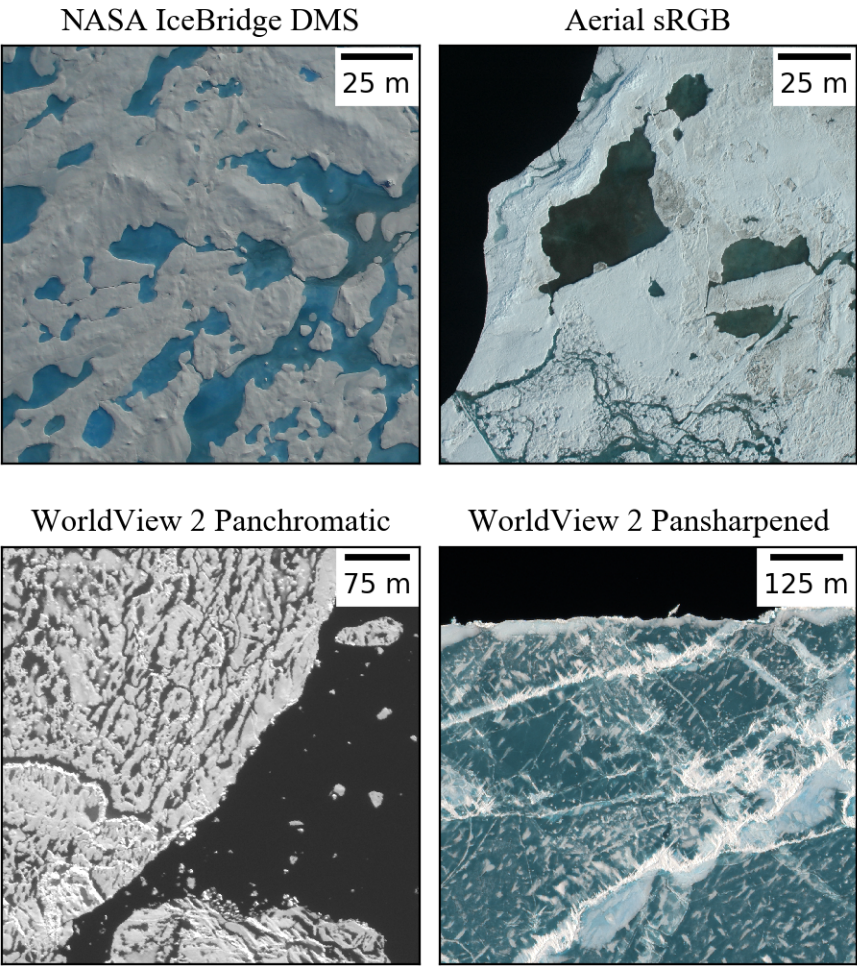
Petty, A. A., Tsamados, M. C., Kurtz, N. T., Farrell, S. L., Newman, T., Harbeck, J. P., Feltham, D. L. and Richter-Menge, J. A.: Characterizing Arctic sea ice topography using high-resolution IceBridge data, *Cryosph.*, 10(3), 1161–1179, doi:10.5194/tc-10-1161-2016, 2016.

Pistone, K., Eisenman, I. and Ramanathan, V.: Observational determination of albedo decrease caused by vanishing Arctic sea ice, *Proc. Natl. Acad. Sci.*, 111(9), 3322–3326, doi:10.1073/pnas.1318201111, 2014.

Polashenski, C., Perovich, D. and Courville, Z.: The mechanisms of sea ice melt pond formation and evolution, *J. Geophys. Res. Ocean.*, 117(C1), n/a-n/a, doi:10.1029/2011JC007231, 2012.

Renner, A. H. H., Gerland, S., Haas, C., Spreen, G., Beckers, J. F., Hansen, E., Nicolaus, M. and Goodwin, H.: Evidence of Arctic sea ice thinning from direct observations, *Geophys. Res. Lett.*, 41(14), 5029–5036, doi:10.1002/2014GL060369, 2014.

- Rösel, A. and Kaleschke, L.: Comparison of different retrieval techniques for melt ponds on Arctic sea ice from Landsat and MODIS satellite data, *Ann. Glaciol.*, 52(57), 185–191, doi:10.3189/172756411795931606, 2011.
- Rösel, A., Kaleschke, L. and Birnbaum, G.: Melt ponds on Arctic sea ice determined from MODIS satellite data using an artificial neural network, *Cryosph.*, 6(2), 431–446, doi:10.5194/tc-6-431-2012, 2012.
- Stroeve, J. C., Serreze, M. C., Holland, M. M., Kay, J. E., Malanik, J. and Barrett, A. P.: The Arctic’s rapidly shrinking sea ice cover: a research synthesis, *Clim. Change*, 110, 1005–1027, doi:10.1007/s10584-011-0101-1, 2012.
- Stroeve, J. C., Markus, T., Boisvert, L., Miller, J. and Barrett, A.: Changes in Arctic melt season and implications for sea ice loss, *Geophys. Res. Lett.*, 41, 1216–1225, doi:10.1002/2013GL058951.Received, 2014.
- Tschudi, M. A., Maslanik, J. A. and Perovich, D. K.: Derivation of melt pond coverage on Arctic sea ice using MODIS observations, *Remote Sens. Environ.*, 112(5), 2605–2614, doi:10.1016/j.rse.2007.12.009, 2008.
- van der Walt, S., Schönberger, J. L., Nunez-Iglesias, J., Boulogne, F., Warner, J. D., Yager, N., Gouillart, E. and Yu, T.: scikit-image: image processing in Python, *PeerJ*, 2, e453, doi:10.7717/peerj.453, 2014.
- Webster, M. A., Rigor, I. G., Perovich, D. K., Richter-menge, J. A., Polashenski, C. M. and Light, B.: Seasonal evolution of melt ponds on Arctic sea ice, *J. Geophys. Res. Ocean.*, 120(9), 1–15, doi:10.1002/2015JC011030.Received, 2015.
- Yan, G., Mas, J. -F., Maathuis, B. H. P., Xiangmin, Z. and Van Dijk, P. M.: Comparison of pixel-based and object-oriented image classification approaches—a case study in a coal fire area, Wuda, Inner Mongolia, China, *Int. J. Remote Sens.*, 27(18), 4039–4055, doi:10.1080/01431160600702632, 2006.



759
760 **Figure 1.** Examples of imagery from each of the four imaging platforms that we seek to classify in this study. Each type of
761 imagery has either a different spatial resolution or and different levels spectral information available.

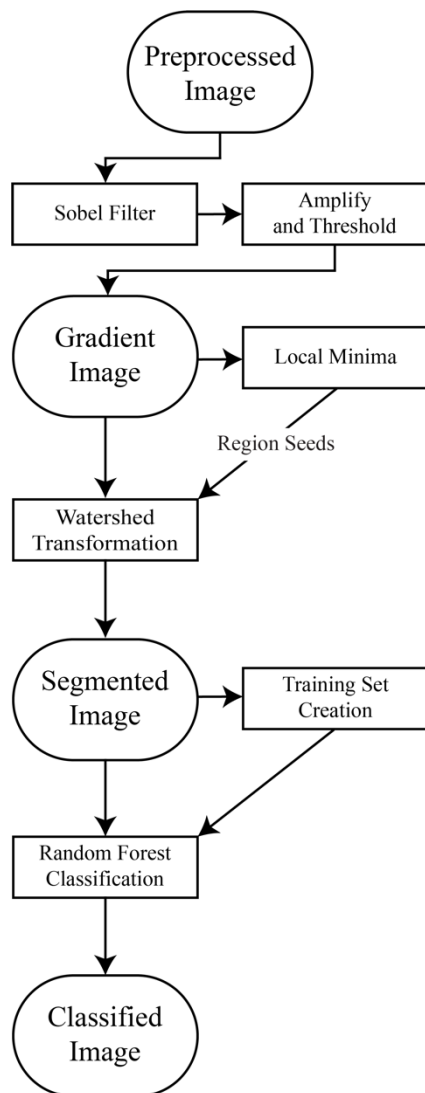


Figure 2. Flow diagram depicting the steps taken to classify an image in the OSSP algorithm.

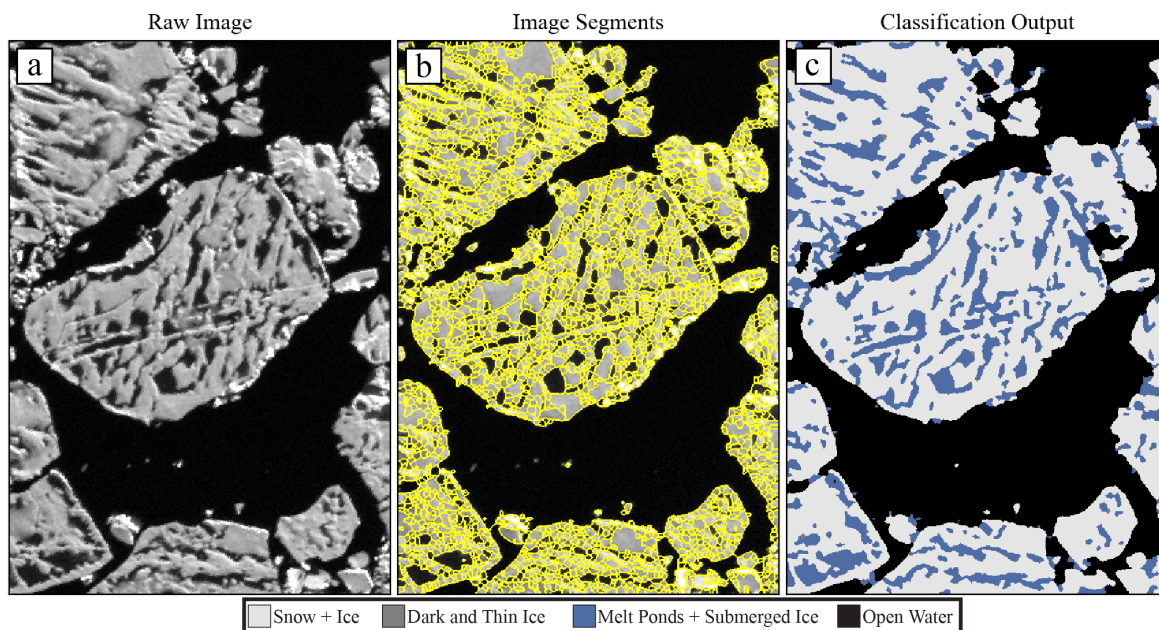


Figure 3. Visual representation of important steps in the image processing workflow. Panel (a) shows preprocessed panchromatic WorldView 2 satellite imagery, taken on July 1, 2014. In panel (b), outlines of the image objects created by our edge detection and watershed transformation are shown overlain on top of the image in panel (a). Panel (c) shows the result of replacing each object with a value corresponding to the prediction of the random forest classifier.

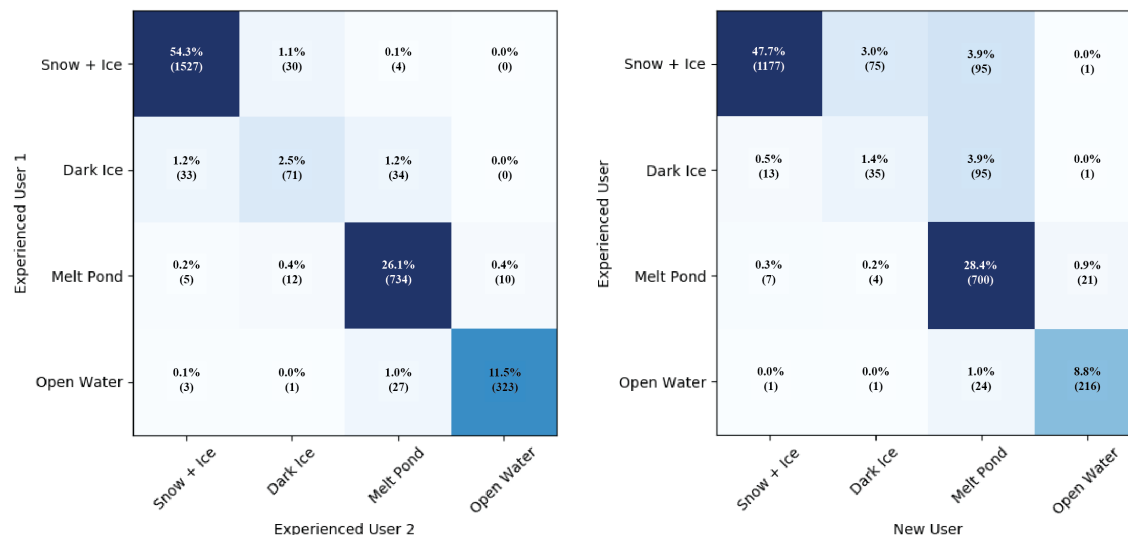


Figure 4. Confusion matrices comparing classification tendencies between two users experienced with the image processing algorithm (left) and between an experienced user and a new user (right). Squares are colored based on the value of the cell, with darker colors indicating more matches. Values along the diagonal of each confusion matrix represents the agreement between each user, while values in off-diagonal regions represent disagreement.

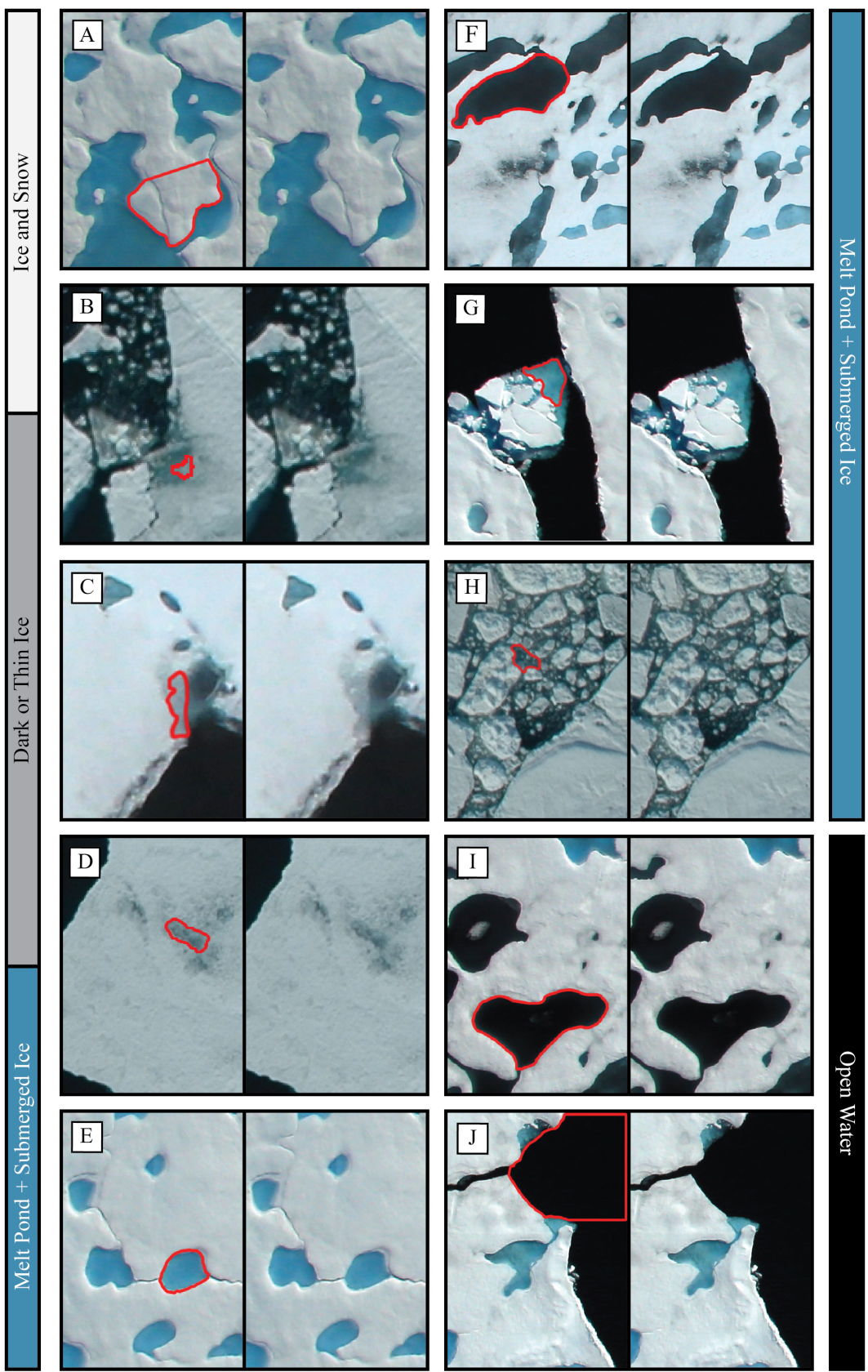


Figure 5. Examples of surfaces seen in aerial imagery of sea ice that span our four classification categories. Panel A: snow covered surface. Panel B: Ice with a thin surface scattering layer where disagreement on true classification exists - represents a small fraction of total surface area. Panel C: Panel D: Surface transitioning to a melt pond that is not yet fully submerged. Panel E: Melt pond. Panel F: Dark melt pond that has not completely melted through. Panel G: Submerged ice. Panel H: Brash, mostly submerged, included in the melt pond category. Panel I: Melt pond that has completely melted through to open water. Panel J: Open water.

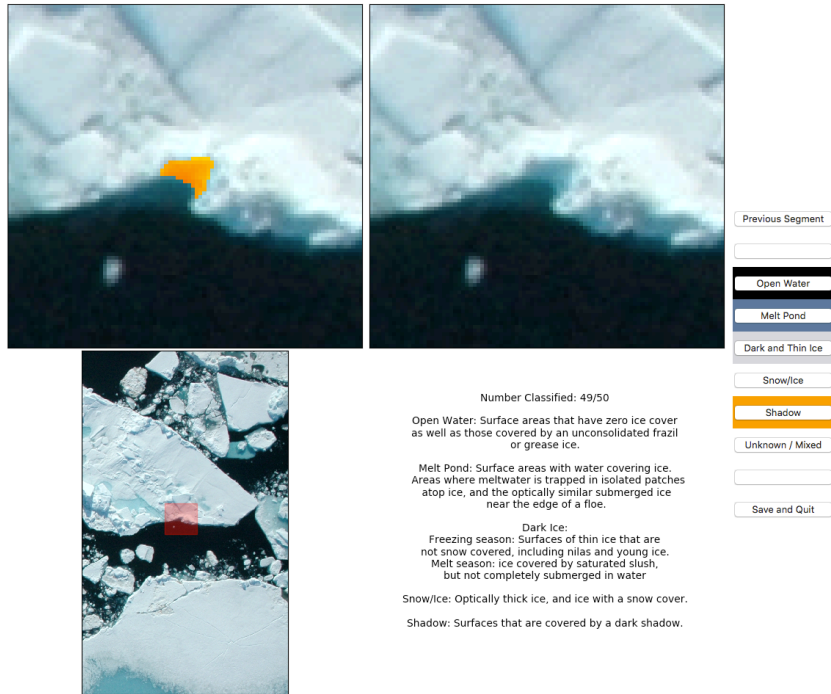


Figure 6. Graphical user interface used to create training datasets and to assess the accuracy of a classified image. Bottom left panel shows an overview of the region to provide the user with spatial context. Top left magnifies the image and highlights the segment of interest, while top right shows the same region with no segment overlap. The user is allowed to choose between any of the relevant surface categories, or to indicate that they are unsure of the classification. As shown, the user interface is demonstrating the classification of a segment for use in a training set. This same GUI is also capable of asking a user to classify an individual pixel, which can be compared to the final classified image for determining accuracy (section 3.6).

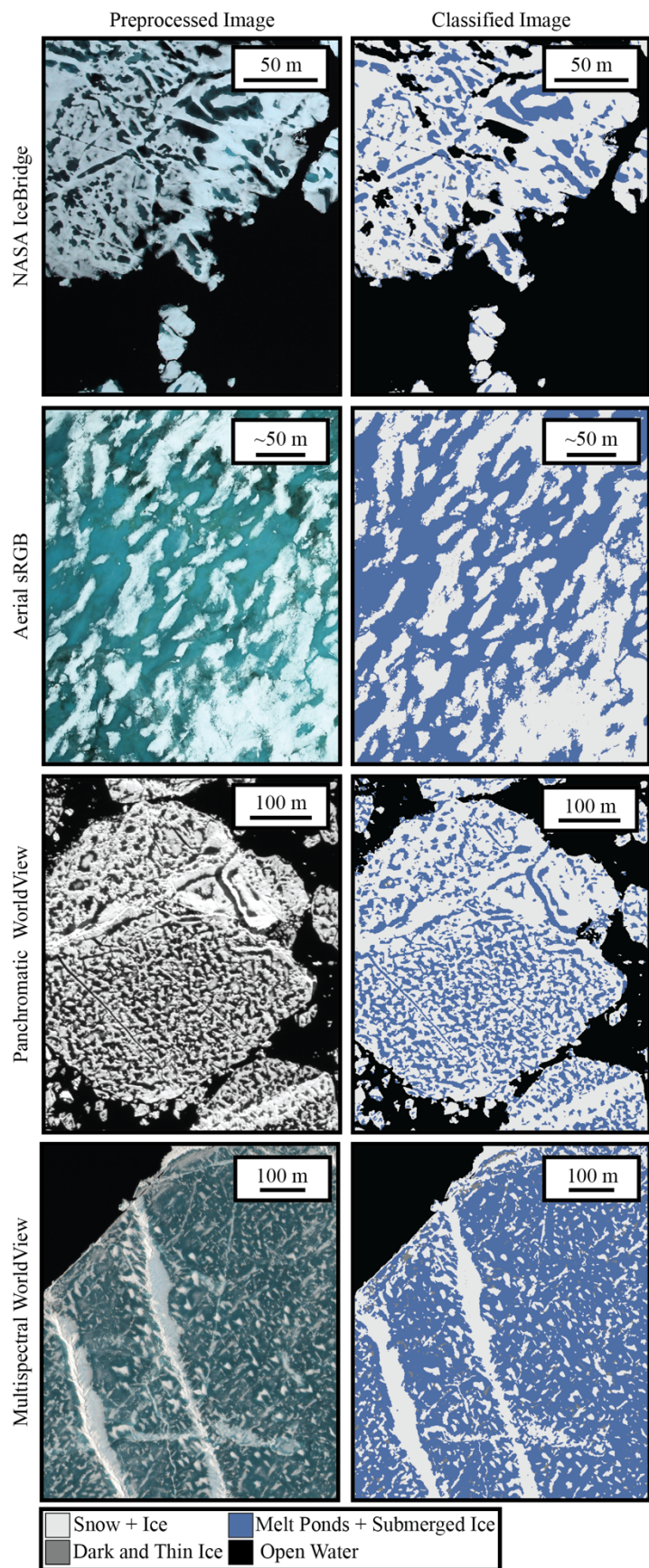


Figure 7. Side-by-side comparison of preprocessed imagery (left) and the result of classification (right) for each of the four imaging platforms. Images depict ice surfaces in varying stages of melt. The NASA IceBridge image, for example, is in very late stages of melt ponds that have already melted through to the ocean.

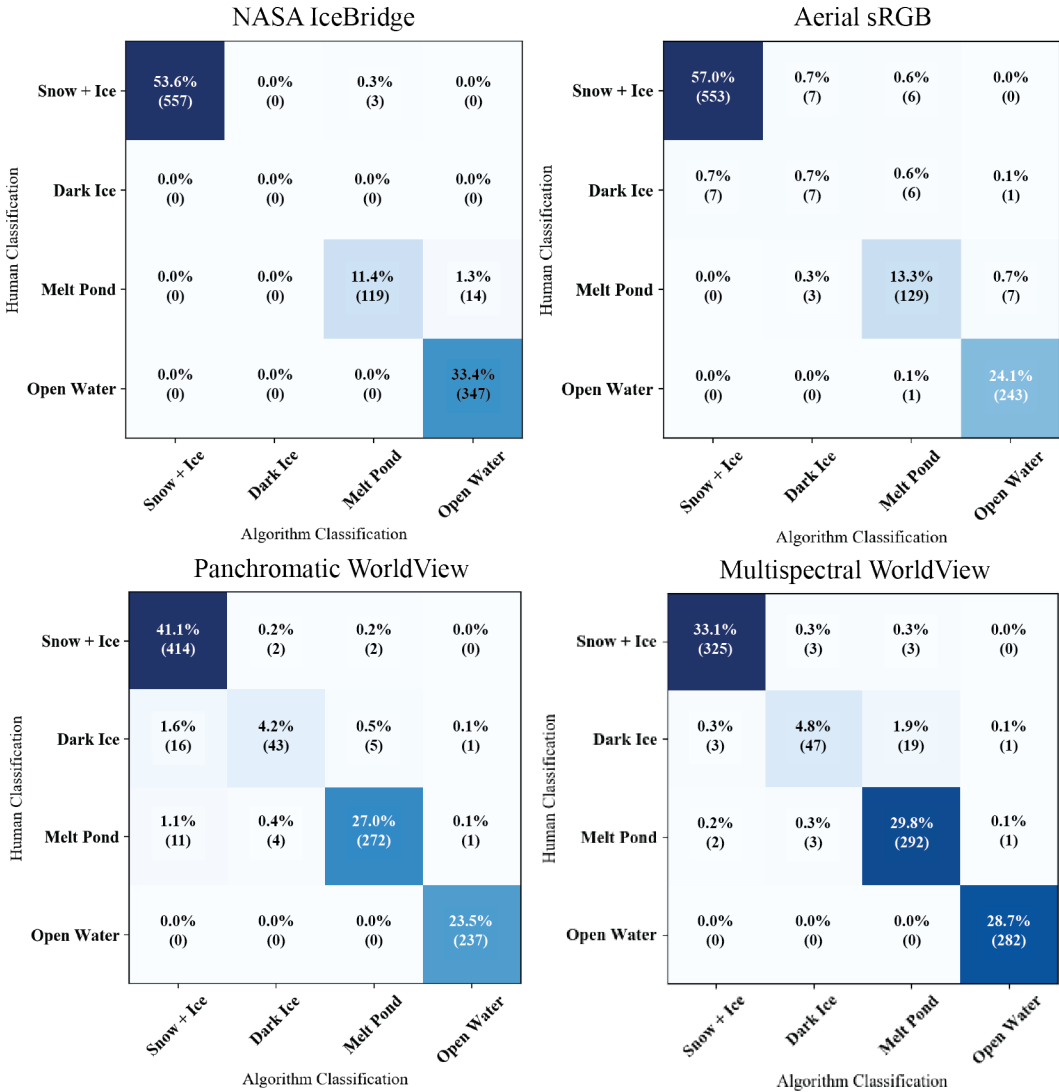


Figure 8. Accuracy confusion matrices comparing the classification of 1000-pixels between a human and the algorithm. Squares are colored based on the value of the cell, with darker colors indicating more matches. Values along the diagonal of each confusion matrix represents the agreement between each classifier, while values in off-diagonal regions represent disagreement.

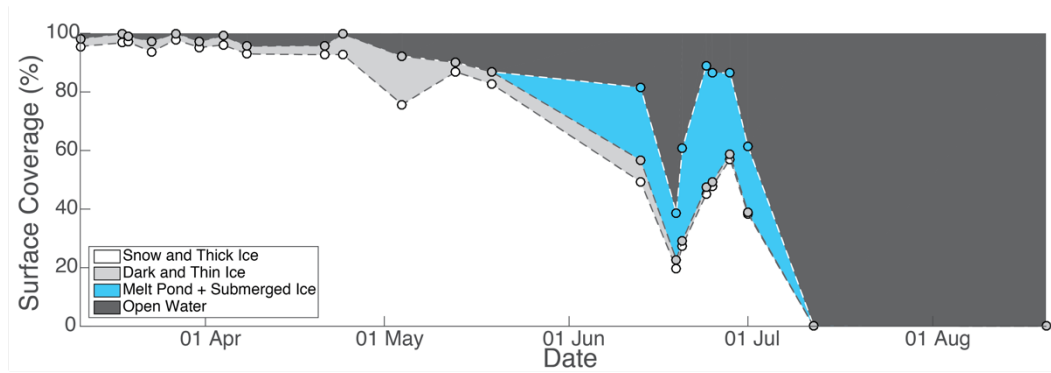


Figure 9. Seasonal progression of surface type distributions at the satellite image collection site; 2014 in the Beaufort Sea at 72°N 128°W. This site represents a Eulerian observation of the sea ice surface, and does not track a floe across its lifetime. Average scene size was 956km² with a minimum of 304km² and a maximum of 1321km².

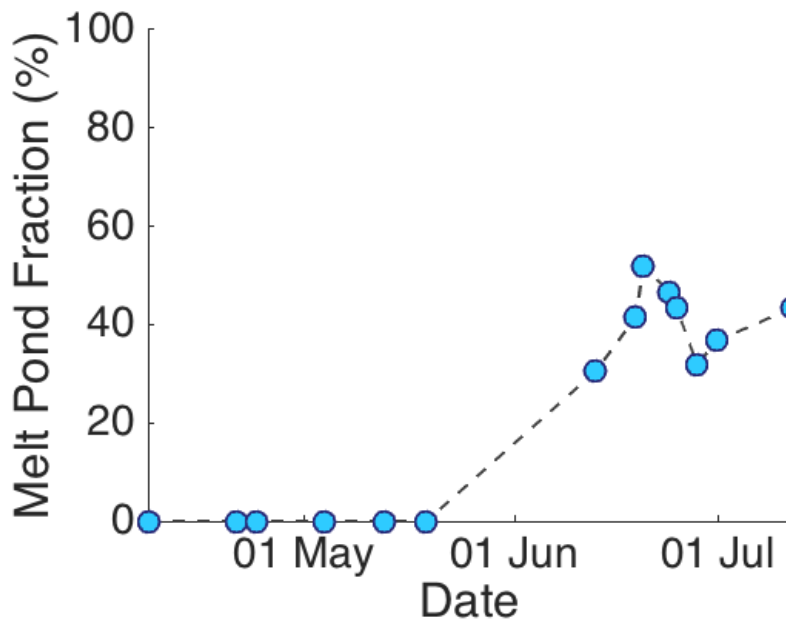


Figure 10. Evolution of melt pond fraction over the 2014 season at our satellite image collection site; 2014 in the Beaufort Sea at 72°N 128°W. This site represents a Eulerian observation of the sea ice surface, and does not track a floe across its lifetime. By August, the sea ice extent has retreated north of this location, and we therefore do not capture a full melt pond cycle.

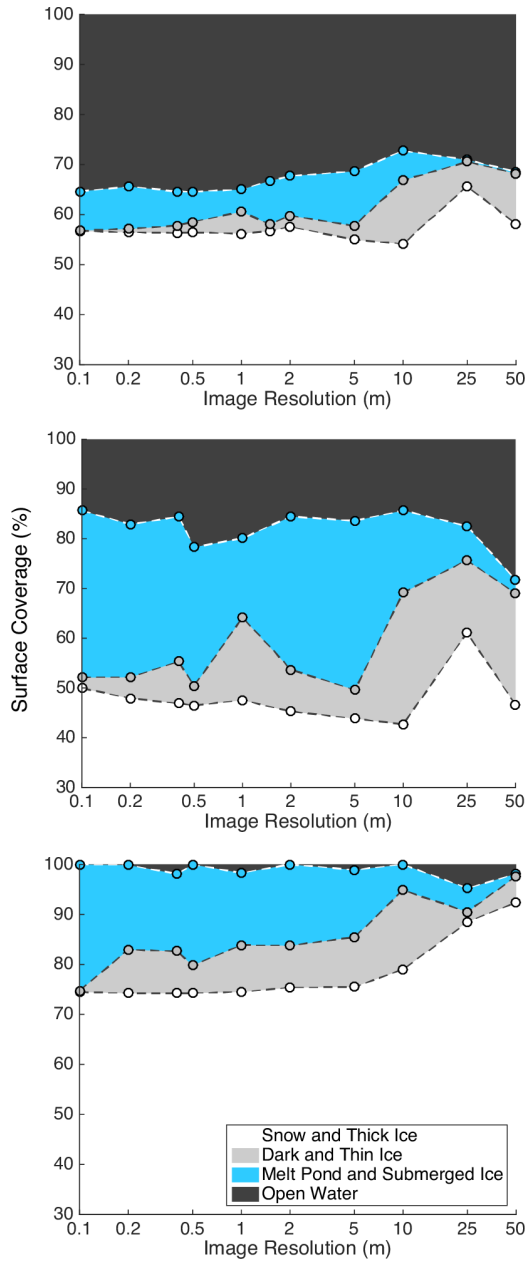


Figure 11. Change in surface coverage percentage as a result of downsampling three IceBridge images. Each plot represents a single image, with resolution along the x-axis on a log scale. Imagery starts at the nominal IceBridge resolution of 0.1m and is degraded to a maximum of 50m.

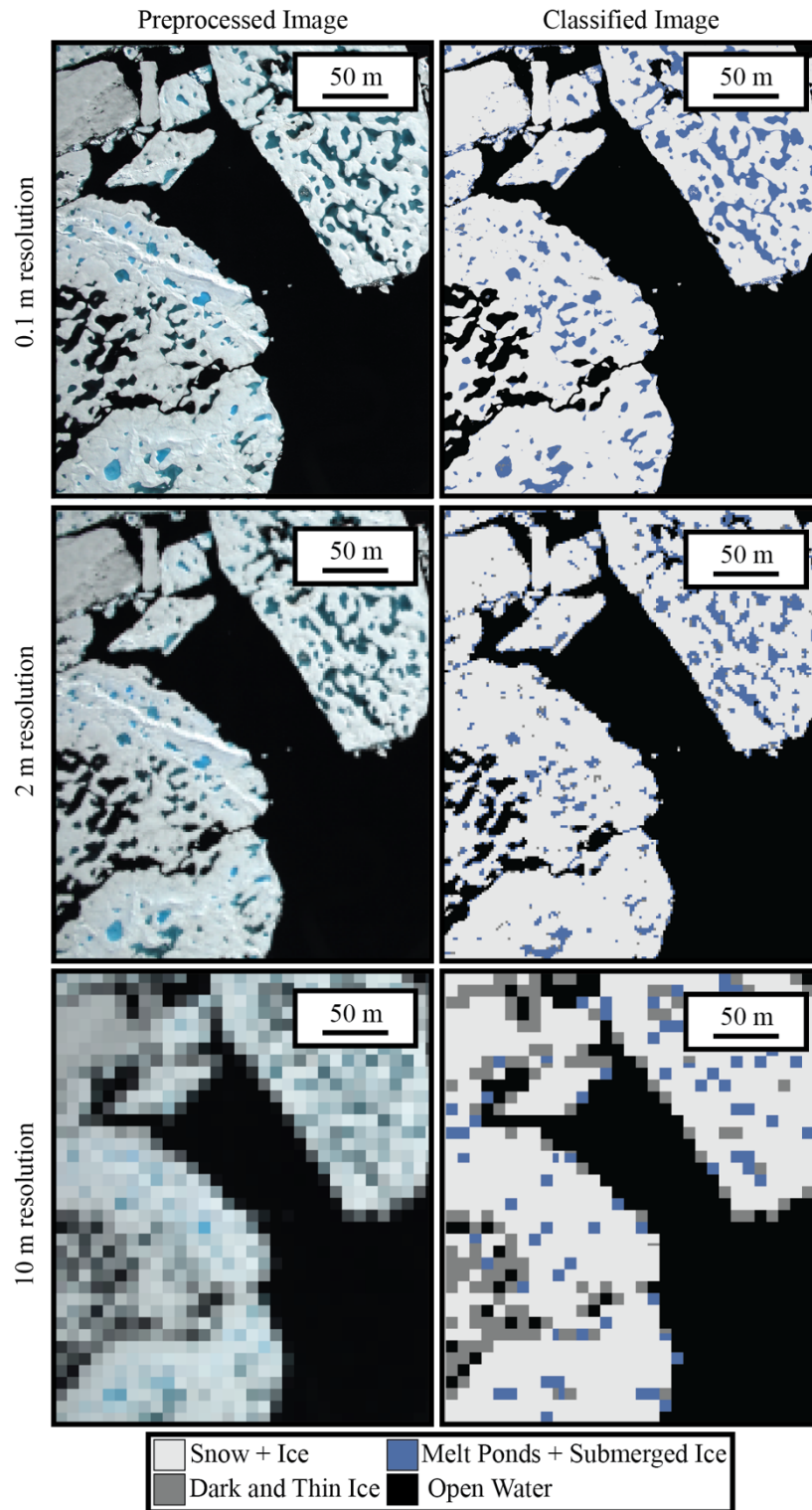


Figure 12. Visual demonstration of the downsampling effect on a single NASA IceBridge image. The top image is shown at the original 0.1 m resolution. The middle image is a resolution of 2m - the equivalent of a multispectral WorldView 2 image without pansharping. The bottom has a resolution of 10m, where pixel size has begun to exceed the average melt pond size.

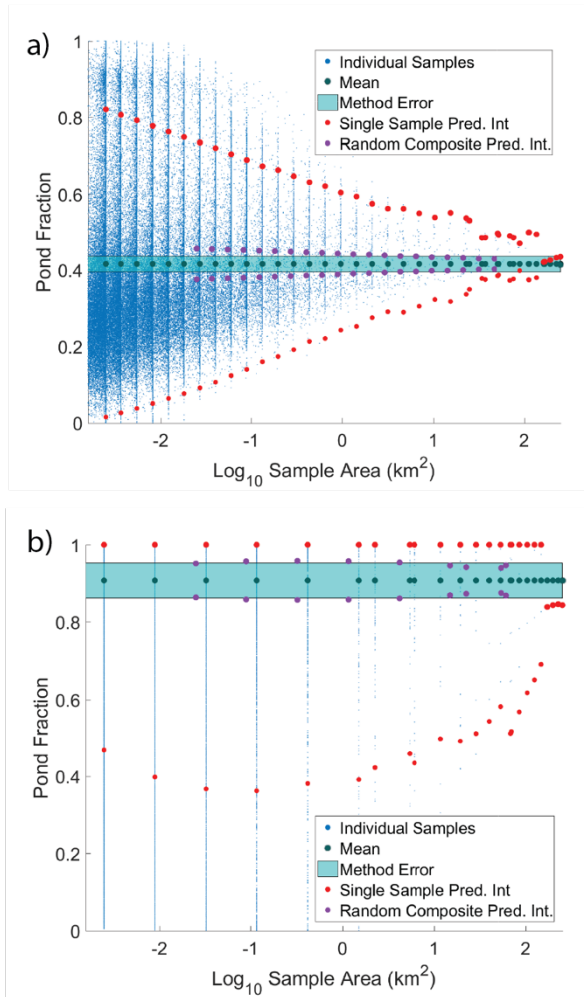


Figure 13. Convergence of melt pond fraction (a) and ice fraction (b) for a WorldView image collected 25 June 2014 at 72°N 128°W as the area evaluated is increased. Small blue dots represent individual image subsets. For segments of a given size, black dots represent the mean value of those samples, red dots represent the 95% prediction interval, and purple dots show the 95% prediction interval for the same total area, but calculated from 100 randomly placed, smaller, samples. Cyan shaded area represents the error in determination expected from the processing method.

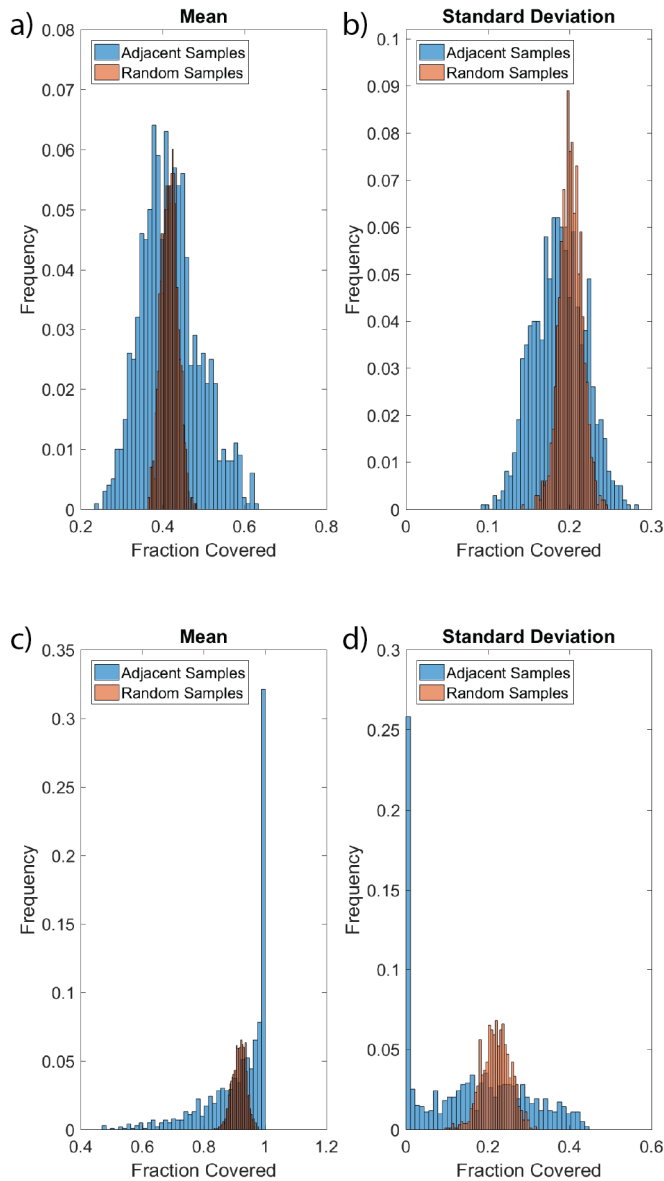


Figure 14. Histogram of mean (a) and standard deviation (b) of 1000 melt pond fraction estimates, each calculated from 100 sample areas on a 25 June 2014 WorldView image. The 100 samples were either randomly distributed across the image (red) or adjacent to each other (blue). Panels (c) and (d) show the same as (a) and (b), respectively, for ice fraction rather than melt pond fraction.

Attribute	MS	PAN	Aerial
Mean (Pan)			
Mean (Coastal)			
Mean (Blue)			
Mean (Green)			
Mean (Yellow)			
Mean (Red)			
Mean (Red Edge)			
Mean (NIR1)			
Mean (NIR2)			
Median (Pan)			
StDev (Pan)			
Min Intensity (Pan)			
Max Intensity (Pan)			
StDev (Blue)			
StDev (Green)			
StDev (Red)			
Entropy			
Segment Size			
Image Date			
Coastal / Green			
Blue / NIR1			
Green / NIR1			
Yellow / Red Edge			
Yellow / NIR1			
Yellow / NIR2			
Red / NIR1			
$(B1 - NIR1)/(B2 + NIR1)$			
$(G - R)/(G + R)$			
$(B - R)/(B + R)^1$			
$(B - G)/(B + G)^1$			
$(G - R)/(2*B - G - R)^1$			
Neighbor Mean			
Neighbor StDev			
Neighbor Max			
Neighbor Entropy			

840 ¹Miao et al. 2015

841 **Table 1. Attributes used for classifying each of the three image types. Blue squares indicate attributes that were used for**
842 **that image. Dark gray squares indicate attributes that are available, but were not found to be sufficiently beneficial in the**
843 **classification to merit inclusion under our criteria. Light gray squares indicate attribute that are not available on that image**
844 **type (e.g. band ratios on a panchromatic image). NIR is the near infrared wavelength. B1 is the coastal WorldView band,**
845 **and B2 is the blue band. R, G, and B, stand for red, green, and blue, respectively.**

Image ID	Sensor Type	Date Collected	Ice + Snow	DTI	MPS	OW	Accuracy
102001002C214D00	Panchromatic	11-Mar-14	96	3	0	2	97
103001002E8F0D00	Panchromatic	18-Mar-14	97	3	0	0	97
102001002BBA0C00	Panchromatic	19-Mar-14	97	2	0	1	96
103001002FC75200	Panchromatic	23-Mar-14	94	4	0	3	95
102001002CB77C00	Panchromatic	27-Mar-14	98	2	0	0	100
1030010030403A00	Panchromatic	31-Mar-14	95	2	0	3	98
1030010031B65000	Panchromatic	4-Apr-14	96	3	0	1	99
102001002BA6C100	Panchromatic	8-Apr-14	93	3	0	4	100
103001002F79A700	Panchromatic	21-Apr-14	93	3	0	4	98
1030010030371B00	Panchromatic	24-Apr-14	93	7	0	0	98
103001003102A600	Panchromatic	4-May-14	76	16	0	8	98
102001003007FA00	Panchromatic	13-May-14	87	3	0	10	97
10300100306F2E00	Panchromatic	19-May-14	83	4	0	13	96
102001003035D700	Panchromatic	13-Jun-14	49	7	25	18	95
1030010033AAC400	Panchromatic	19-Jun-14	20	3	16	61	97
1020010031DF9E00	Panchromatic	20-Jun-14	27	2	31	39	96
1020010032B94E00	Panchromatic	24-Jun-14	45	2	41	11	95
102001003122A700	Panchromatic	25-Jun-14	48	1	37	13	97
102001002F4F1A00	Panchromatic	28-Jun-14	57	2	28	14	95
10300100346D1200	Panchromatic	1-Jul-14	38	0	23	39	97
1030010035C8D000	Panchromatic	12-Jul-14	0	0	0	100	100
103001003421AB00	Panchromatic	20-Aug-14	0	0	0	100	100
10300100324B7D00	Multispectral	13-Jun-14	44	7	29	19	96
1030010033AAC400	Multispectral	19-Jun-14	16	3	19	62	97
10300100346D1200	Multispectral	1-Jul-14	44	2	26	28	98
1030010035C8D000	Multispectral	12-Jul-14	0	0	0	100	100
2016_07_13_05863	IceBridge	13-Jul-16	50	2	34	14	92
2016_07_13_05882	IceBridge	13-Jul-16	72	1	26	0	97
2016_07_13_05996	IceBridge	13-Jul-16	70	2	28	0	95
2016_07_13_06018	IceBridge	13-Jul-16	61	2	36	1	91
2016_07_13_06087	IceBridge	13-Jul-16	66	1	33	0	99
2016_07_16_00373	IceBridge	16-Jul-16	9	0	2	89	100
2016_07_16_00385	IceBridge	16-Jul-16	66	1	14	20	98

2016_07_16_00662	IceBridge	16-Jul-16	49	1	16	35	98
2016_07_16_00739	IceBridge	16-Jul-16	67	2	25	6	97
2016_07_16_01569	IceBridge	16-Jul-16	22	0	7	71	97
2016_07_16_02654	IceBridge	16-Jul-16	35	0	10	54	95
2016_07_19_01172	IceBridge	19-Jul-16	62	0	14	24	90
2016_07_19_01179	IceBridge	19-Jul-16	57	0	10	32	95
2016_07_19_02599	IceBridge	19-Jul-16	51	0	7	43	99
2016_07_19_02603	IceBridge	19-Jul-16	69	0	9	22	99
2016_07_19_02735	IceBridge	19-Jul-16	74	0	25	0	100
2016_07_19_03299	IceBridge	19-Jul-16	57	0	8	35	96
2016_07_21_01221	IceBridge	21-Jul-16	49	0	4	47	97
2016_07_21_01311	IceBridge	21-Jul-16	87	1	5	7	95
2016_07_21_01316	IceBridge	21-Jul-16	92	0	4	4	99
DSC_0154	Aerial sRGB	8-Jun-09	43	4	53	0	94
DSC_0327	Aerial sRGB	8-Jun-09	33	3	63	0	90
DSC_0375	Aerial sRGB	8-Jun-09	96	0	4	0	99
DSC_0422	Aerial sRGB	8-Jun-09	88	0	11	0	98
DSC_0223	Aerial sRGB	10-Jun-09	46	1	53	0	93
DSC_0243	Aerial sRGB	10-Jun-09	59	1	40	1	98
DSC_0314	Aerial sRGB	10-Jun-09	89	0	11	0	95
DSC_0319	Aerial sRGB	10-Jun-09	75	2	19	4	88
DSC_0323	Aerial sRGB	10-Jun-09	37	2	61	0	95
DSC_0338	Aerial sRGB	10-Jun-09	83	2	15	1	95
DSC_0386	Aerial sRGB	10-Jun-09	80	3	14	3	89
DSC_0394	Aerial sRGB	10-Jun-09	79	2	10	9	95
DSC_0412	Aerial sRGB	10-Jun-09	63	2	24	10	92
DSC_0425	Aerial sRGB	10-Jun-09	56	2	17	24	97
DSC_0439	Aerial sRGB	10-Jun-09	71	1	6	22	98
DSC_0441	Aerial sRGB	10-Jun-09	57	0	4	38	98
DSC_0486	Aerial sRGB	10-Jun-09	53	1	17	29	96
DSC_0634	Aerial sRGB	10-Jun-09	72	1	14	12	96
DSC_0207	Aerial sRGB	13-Jun-09	80	1	19	0	96
DSC_0514	Aerial sRGB	13-Jun-09	86	1	13	0	97

Results Table 2. The complete results of imagery processed for this analysis. Descriptions for each image includes the image type, date collected, the percent of the image that falls into each of the four categories, and the accuracy assessment.

Image Source	Training Dataset Size	Out-of-bag Error
Panchromatic WorldView	1000	0.94
Pansharpened WorldView	859	0.89
Aerial Imagery	945	0.94
IceBridge Imagery	940	0.91

Table 3. Out-of-Bag scores for the three training datasets used to classify imagery from each of the four sensor platforms, and the number of objects manually classified for each set.